

HATNET VARIABILITY SURVEY IN THE HIGH STELLAR DENSITY “KEPLER FIELD” WITH MILLIMAGNITUDE IMAGE SUBTRACTION PHOTOMETRY

J. D. HARTMAN, G. BAKOS,^{1,2} K. Z. STANEK, AND R. W. NOYES

Harvard-Smithsonian Center for Astrophysics, 60 Garden Street, Cambridge, MA 02138; jhartman@cfa.harvard.edu,
gbakos@cfa.harvard.edu, kstanek@cfa.harvard.edu, rnoyes@cfa.harvard.edu

Received 2004 June 1; accepted 2004 July 1

ABSTRACT

The Hungarian-made Automated Telescope Network (HATnet) is an ongoing project to detect transiting extrasolar planets using small-aperture (11 cm diameter) robotic telescopes. In this paper, we present the results from using image subtraction photometry to reduce a crowded stellar field observed with one of the HATnet telescopes (HAT-5). This field was chosen to overlap with the planned *Kepler* mission. We obtained *I*-band light curves for 98,000 objects in a 67 square degree field of view centered at J2000 (α, δ) = (19^h44^m00^s.0, +37°32'00") near the Galactic plane in the constellations Cygnus and Lyra. These observations include 788 exposures of 5 minutes’ length over 30 days. For the brightest stars ($I \sim 8.0$) we achieved a precision of 3.5 mmag, falling to 0.1 mag at the faint end ($I \sim 14$). From these light curves we identify 1617 variable stars, of which 1439 are newly discovered. The fact that nearly 90% of the variables were previously undetected further demonstrates the vast number of variables yet to be discovered even among fairly bright stars in our Galaxy. We also discuss some of the most interesting cases. These include V1171 Cyg, a triple system with the inner two stars in a $P = 1.462$ day period eclipsing orbit and the outer star a $P = 4.86$ day Cepheid; HD 227269, an eccentric eclipsing system with a $P = 4.86$ day period that also shows $P = 2.907$ day pulsations; WW Cyg, a well-studied eclipsing binary; V482 Cyg, an R Coronae Borealis star; and V546 Cyg, a PV Telescopii variable. We also detect a number of small-amplitude variables, in some cases with full amplitude as low as 10 mmag.

Key words: binaries: eclipsing — catalogs — Cepheids — δ Scuti — stars: variables: other — techniques: photometric

Online material: color figures, machine-readable table

1. INTRODUCTION

The Hungarian-made Automated Telescope network (HATnet) is an ongoing project to detect transiting extrasolar planets using small-aperture (11 cm diameter) robotic telescopes (Bakos et al. 2004, hereafter B04). The HATnet telescopes make use of a fast focal ratio ($f/1.8$) to efficiently monitor a large number of fairly bright stars ($I < 14.5$) over a wide field of view (FOV). A number of other groups have also taken this small-telescope approach toward finding transits (see Horne 2003 for a comprehensive list). In contrast, there are several groups that employ a “narrow, but deep” method. This includes the transit search by the Optical Gravitational Lensing Experiment (OGLE) project, which to date has discovered three confirmed “very hot Jupiters” (Udalski et al. 2002, 2003; Konacki et al. 2003; Torres et al. 2004; Bouchy et al. 2004; Konacki et al. 2004), the only planets detected so far by transit searches.

Besides the size of the telescopes and FOV, another difference between the approaches is the method used to obtain photometry for the monitored stars. For several years, many of the “narrow and deep” searches have made use of the image subtraction techniques due to Alard & Lupton (1998; see also Alard 2000). This includes OGLE, which uses difference image analysis (Woźniak 2000), and PISCES (Mochejska et al. 2002, 2004), which uses a different implementation of image subtraction in monitoring the open clusters NGC 2158 and NGC 6791.

Image subtraction is the current state of the art for massive time series photometry. It has been shown that in narrow, dense fields, it can produce light curves with precision down to the photon limit (see, e.g., Mochejska et al. 2002). However, to date there exist no published results that use image subtraction in a wide-field setting. This has limited these searches to observing only relatively isolated stars in regions where point-spread function (PSF) fitting and aperture photometry yield high precision.

In this paper, we report our use of image subtraction to obtain light curves for 98,000 objects in a single field, near the Galactic plane, observed with one of the HATnet telescopes (HAT-5). This field was chosen in particular because of its overlap with NASA’s *Kepler* mission to observe transiting planets from space (Borucki et al. 2003). Over 9000 of the brightest light curves have an rms of less than 1% (i.e., better than 10 mmag precision) at 5 minute sampling. In the following section we describe our observations, and in § 3 we discuss our image subtraction-based data reduction to obtain the light curves.

While the main purpose of HATnet remains the discovery of transiting extrasolar planets, it is also useful for discovering and characterizing variable stars in the Galaxy. To this end, we have analyzed these light curves to select a list of 1617 variable stars, of which 1439 are newly discovered. We describe our selection criteria in § 4 and present our catalog, including a discussion of many interesting cases, in § 5. We finish with a brief summary of our results in § 6.

2. OBSERVATIONS

The data were obtained in 2003 June and July using the HAT-5 telescope located at the Fred Lawrence Whipple

¹ Predoctoral Fellow, Smithsonian Astrophysical Observatory.

² Also Konkoly Observatory, Pf. 67, H-1525 Budapest, Hungary.

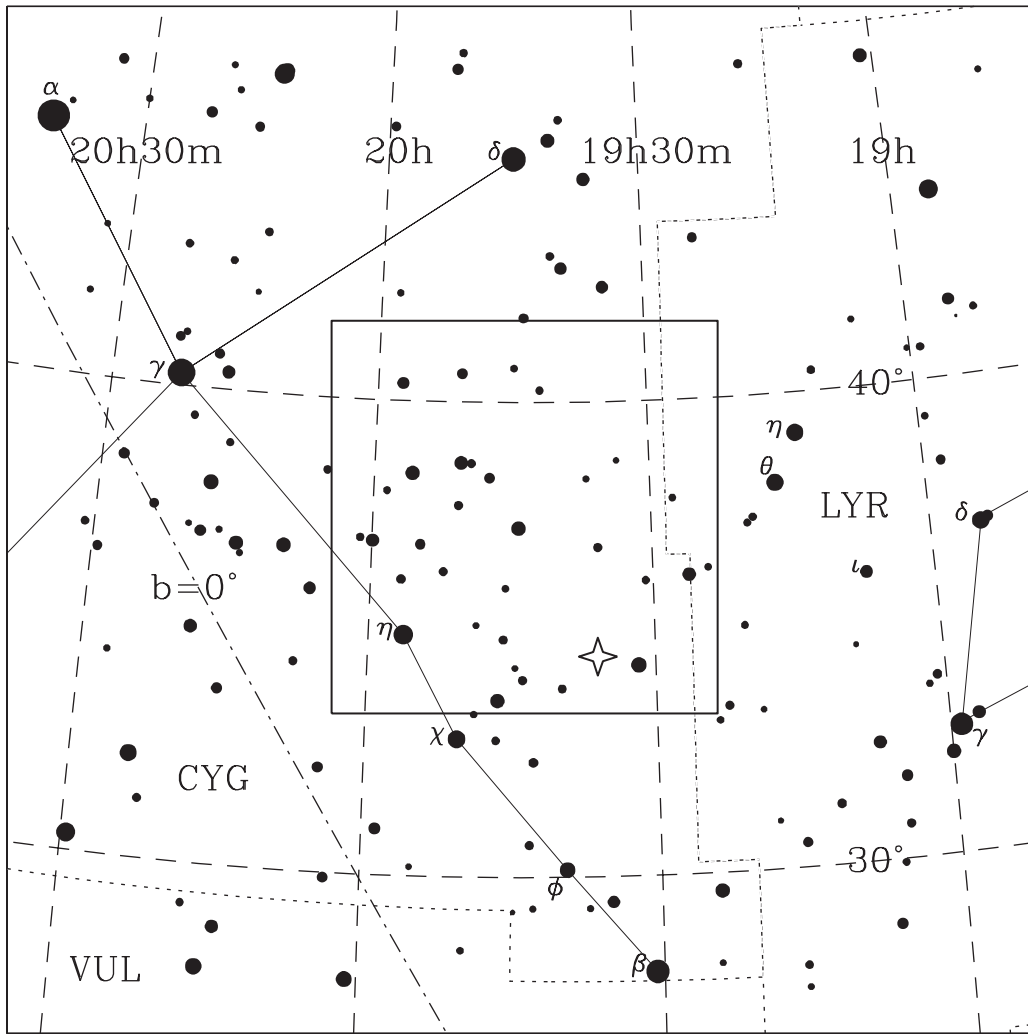


Fig. 1.—The observed 8.3×8.3 field of view, lying at the western boundary of Cygnus. The proposed center of the *Kepler* mission is marked with a star. The plane of the Galactic disk is shown with the dot-dashed line.

Observatory (FLWO). The telescope uses a Canon 11 cm diameter f/1.8L lens and a Cousins *I*-band filter to image onto an Apogee AP10 front-illuminated 2K \times 2K CCD. The result is an 8.3×8.3 FOV image with a pixel scale of $14''$. For details on the design and performance of the instrument, see B04. The pointing was stepped in a prescribed pattern of subpixel increments during each exposure to broaden the full width at half-maximum (FWHM) of the stellar profiles from ~ 1.5 to ~ 2.5 pixels.

The field we observed (HAT 199) is centered at J2000 (α, δ) = (19 $^{\text{h}}44^{\text{m}}00^{\text{s}}.0$, +37 $^{\circ}32'00''.0$) and lies at the western boundary of the constellation Cygnus (Fig. 1). The southeastern corner of the field (*lower left*) is within 2° of the Galactic plane. As mentioned above, this field was chosen to overlap with the proposed center for NASA's *Kepler* mission (D. Latham 2004, private communication). Thus, these observations may be useful as a means of identifying interesting objects (including stars bearing transiting planets) to be investigated at higher precision with *Kepler*.

This field contains hundreds of thousands of relatively bright sources, from which we select 98,000 with $I < 14.8$. Just from the sources we select, the density is 0.4 objects per square arcminute. At our pixel scale, this corresponds to one object per 42 pixels, or a typical separation of 6–7 pixels between the

objects. At this density the stellar profiles are highly blended, particularly toward the Galactic plane (Fig. 2). Because of this severe blending, large portions of this field would not be useful for transit searches or precision photometry in general using traditional photometric methods (e.g., simple aperture photometry, or PSF fitting).

3. DATA REDUCTION

3.1. Image Subtraction

The preliminary CCD reductions, including dark current subtraction, flat-fielding, etc., were discussed in B04. To obtain photometry, we used the image subtraction methods due to Alard & Lupton (1998; see also Alard 2000). We describe the procedure here, referring the reader interested in the theoretical basis of the method to the original papers.

The simplest method to measure the apparent magnitude of a star is to measure the total signal within a fixed aperture centered on the star using a constant weight per pixel. However, when one is working on a crowded stellar field this method breaks down, since more than one source will contribute light to the aperture. The typical procedure in this case is to determine a PSF for the frame using bright or isolated stars and then fit that PSF to all the stars on the frame.

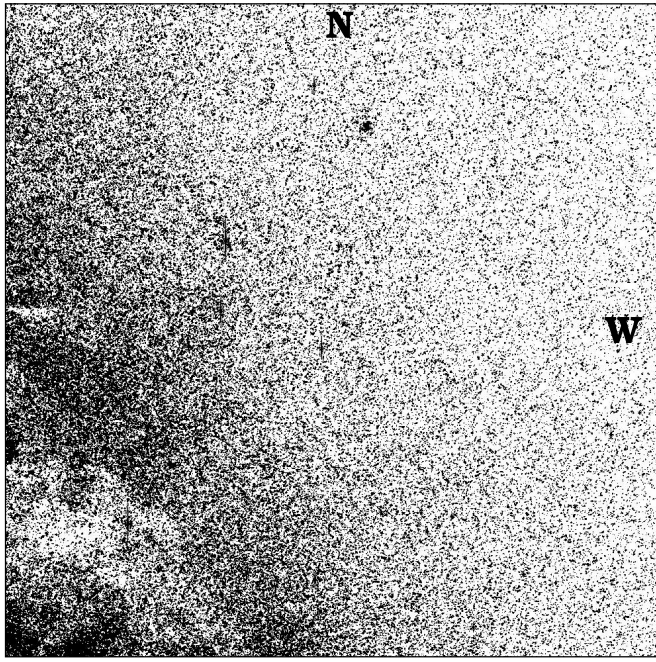


FIG. 2.—Image of the HAT “Kepler field” (HAT 199). Note the very high stellar density, and variable extinction, particularly toward the Galactic disk at lower left.

When obtaining light curves for the stars in a dense field, it is useful to note that on average the intrinsic magnitude of the stars does not change from image to image. Instead of performing PSF fitting separately on every image, one can obtain higher precision by performing weighted aperture photometry on the sparsely populated difference image formed by subtracting the image from a reference image. To do this, one needs a method for matching two images with different PSFs before subtracting so that the subtracted image is not dominated by residuals from the different PSFs. Alard & Lupton (1998) solved this problem by proposing an efficient method for finding a function that transforms the PSF of the reference image into the PSF of the image to be subtracted (the kernel). Their scheme does not assume anything about the shape of the PSF, only that the kernel, which relates the PSFs on different images, can be written in terms of a product of Gaussians and polynomials (of arbitrary order). Alard (2000) modified the procedure to allow for spatial variations in the kernel that can be fitted with a polynomial. When fitting the kernel it is not necessary to use only bright or isolated stars; instead, even stars in the highest density regions contribute to the fit. This is one reason why the kernel can be obtained with better accuracy than an independent determination of the PSF. Another reason why the kernel can be determined with better accuracy than the PSF is that while the PSF can have an arbitrary shape that may not be well fitted by any model function, empirically the kernel relating two PSFs from the same instrument appears to be well fitted by Alard & Lupton’s model, regardless of the shape of the PSF. Moreover, because the method allows for a constant scaling of the kernel, any correlated variations, such as the change in magnitude due to different atmospheric extinction, are automatically removed.

Once the kernel is obtained and the images have been subtracted, it is a simple step to obtain the relative change in magnitude between the subtracted image and the reference

image. This is done by determining a PSF for the reference image, convolving it with the kernel, and then performing weighted aperture photometry on the subtracted image. Since the kernel can be obtained with better accuracy than the PSF, by determining a single PSF and applying it to all the images (after transforming with the kernel) one can achieve higher precision light curves than by determining the PSF of each image separately. Note that this procedure only works in the regime where the PSF can be accurately determined on the reference image. In the limit of an extremely crowded field, one may have to obtain the PSF directly on the subtracted image.

All the above procedures are included in the ISIS 2.1 package.³ There are several references on how to run ISIS; the procedure we follow is similar to that used by Mochejska et al. (2002). We discuss the specifics of our implementation in Appendix A.

3.2. Photometry

There are two approaches that one can take toward obtaining light curves and identifying variables with subtracted images. The first is to co-add the absolute value of the subtracted images and search for strong point-source signals to identify variable stars for which to obtain light curves. The second is to generate a list of stars from the reference image, measure photometry on the subtracted images for a selection of stars on the list, and scan the resulting light curves for variables. Using the former approach, it becomes very difficult to efficiently identify extremely subtle variations, such as those due to a transiting planet, as these tend to get washed out in the overall noise of the image (Mochejska et al. 2002). Since the transit candidates are typically among the sources with the smoothest light curves, it is more efficient to obtain photometry for all the objects and use routines that are optimized for selecting candidates directly from the light curves. For this reason we implement the latter approach. In doing so, we do make two sacrifices: any transient phenomena that do not have a signal in the 47 images combined to make the reference image will go unnoticed, and constant stars located near variable stars will have variable light curves as a result of the nondeblending, weighted aperture photometry performed on the subtracted images by the ISIS routine “phot.csh.” The second problem turns out to be significant for our program, and we describe the steps we have taken to mitigate it in § 4.6. Note that this procedure also requires the ability to generate an input list of stars. Since image subtraction is often able to perform even in the densest fields, when working in an extremely crowded field the former approach may be the only option for identifying variables.

To obtain the list of stars, we used the DAOPHOT/ALLSTAR package (Stetson 1987, 1992). The list contains 98,000 objects ranging in magnitude from $I = 7.79$ down to 14.87. We then obtained light curves for all 98,000 objects using the “phot.csh” routine contained in the ISIS package. We discuss the details of this procedure in Appendix B.

We used the *Hipparcos* main catalog (Perryman et al. 1997) to provide the absolute calibration for our instrumental, I -band, reference magnitudes. Using the coordinates we obtained from matching to the Two Micron All Sky Survey (2MASS; Skrutskie et al. 1997) as discussed in § 3.4, we obtained matches with 55 point sources from *Hipparcos* that also had I -band measurements listed. The I magnitudes listed were all obtained

³ The ISIS package is available from C. Alard’s Web site at <http://www2.iap.fr/users/alard/package.html>.

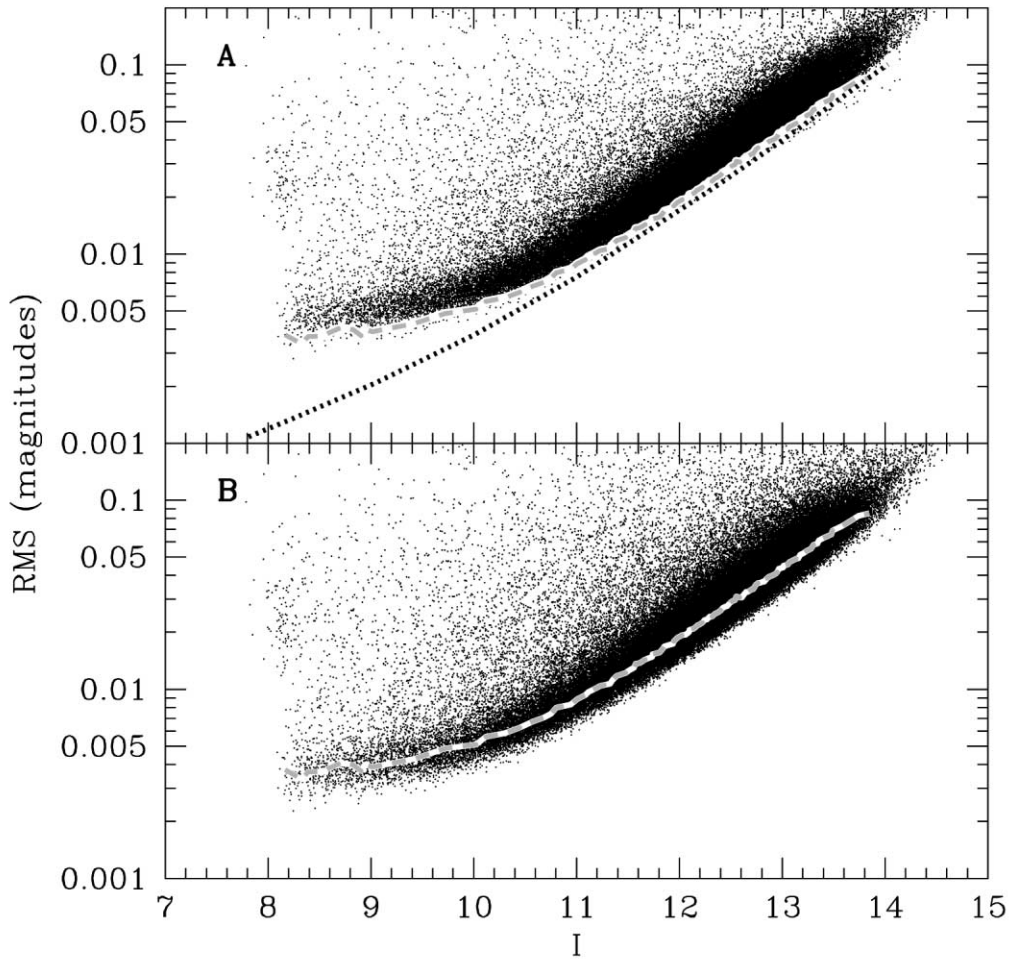


FIG. 3.—(a) The rms vs. I -band magnitude for the 97,540 light curves with rms better than 0.2 mag. The dashed line marks the lower envelope of the plotted distribution. The dotted line shows the theoretical limits (photon noise). (b) The rms vs. I for the light curves binned by 20 minutes. The dashed line is the same as in (a). The fact that binning reduces the rms shows that the light curves are not dominated by systematic errors that are correlated on timescales longer than 20 minutes.

from ground-based measurements, or from transformations of *Hipparcos* measurements in other photometric systems. We find a 1σ uncertainty of ± 0.06 mag on our absolute calibration to *Hipparcos*. This error is likely on the *Hipparcos* side and may be due to the variety of sources for the I -band measurements.

3.3. Photometric Precision

Figure 3 shows the light curve rms versus reference magnitude for our 98,000 objects. Because many of the light curves contain outliers that result from nonrandom errors (satellite crossings, bad pixels, etc.), before calculating the rms of Figure 3a we first sorted each light curve by magnitude and removed two outlier points from each end. From this plot it is clear that we have obtained a photometric precision down to 3.5 mmag at the bright end. For the dim end, the noise is dominated by the background and rises to 0.01 mag at $I \sim 11.3$. This is very close to the results that have been achieved on sparse stellar fields using aperture photometry with the same instrument (see B04). From this we conclude that we can achieve the same precision in a dense field with image subtraction that we can in a sparse field with aperture photometry. The fact that neither method is good down to the photon limit implies that there is some as yet unexplained systematic error that affects both methods. There are a total of 9004 light curves with rms better than 10 mmag, and another 16,540 light curves with rms between 10 and 20 mmag.

Although we achieve very high precision for the brightest stars, it is apparent that we are not photon limited at the bright end. To determine whether or not our systematic errors are correlated along the light curves, we binned the light curves in time using a bin size of 20 minutes. This reduced the maximum number of points per light curve from 784 to 286, a factor of 2.7. If the errors were correlated on timescales longer than 20 minutes, this procedure would not affect the rms of the light curves. But for uncorrelated errors, we would expect the rms to be reduced by 40%. In Figure 3b, we show the resulting σ versus reference I diagram, together with a line tracing the bottom envelope from Figure 3a. At the bright end the rms approaches 2.5 mmag, or a reduction of 29%, which is consistent with the errors being uncorrelated.

3.4. Astrometry

Because the ISIS package provides an image registration routine via “interp.csh,” we do not follow the same steps as B04 to match images to one another. Instead, once we have the (X , Y) positions of all point sources in our field from DAOPHOT, we use the Delaunay triangulation algorithm as described in B04 to match to the Guide Star Catalog 2.2 (Bucciarelli et al. 2001). Using the resulting grid of right ascension and declination for our field, we match our entire list to 2MASS using a matching radius of $10''$. We then adopt the right ascension and declination from 2MASS for the matched sources.

Because 2MASS contains many objects that are much fainter than our upper magnitude limit, and is at higher resolution than our observations, we only match to 2MASS sources with $J < 13$. Even at this cut there are over 170,000 2MASS sources in the field, compared with our 98,000. Taking a cut at fainter magnitude will tend to increase the number of spurious matches between our objects and fainter 2MASS sources. Although the magnitude that we measure for each “object” will be the summed I band of all objects within roughly $30''$, for the purposes of follow-up we will adopt the convention that our “object” lies at the location of the nearest 2MASS source within $10''$ that has $J < 13$.

Using a $10''$ matching radius, we obtain 83,900 matches, with 6174 objects having more than one 2MASS source within $10''$ (multiple matches). For all multiple matches, we choose the closest match as the “real” one. We also matched with smaller radii: for $1''$ there were 16,557 matches, and for $5''$ there were 64,844 matches. To determine whether or not the number of multiple matches is consistent with random matching, we also shifted our entire star list by $15''$ and by $30''$ and matched it to 2MASS. For the $15''$ shift we obtained 6776 matches, and for the $30''$ shift we obtained 4103 matches. If the 170,000 2MASS objects were randomly distributed across the frame, one would expect to find one object for every 24 pixels. Assuming that our 98,000 objects are also randomly distributed, we would expect 6,400 random matches between HAT and 2MASS. This is consistent with the number of multiple matches that we see with the $10''$ matching radius, and with the number of matches that we see with the $15''$ shift. The fact that the number of matches drops as we shift to $30''$ may suggest that the objects are not randomly distributed but have some degree of clustering.

There are a number of objects with $J > 13$ that will not have matches in our catalog. Using the distribution of colors $I-J$ obtained from the 2MASS matches with $10 < I < 11$, we estimate that roughly 5000 of the observed sources with $I > 11$ should have $J > 13$. The fact that 13,920 of the 14,100 unmatched objects have $I > 11$ shows that most of the unmatched objects (~ 9000) cannot be accounted for from the 2MASS cutoff. These sources may be spurious detections by DAOPHOT, or they could be sources with bad astrometry. If we assume that they are spurious, then we can estimate that for $I \sim 12.5$ approximately 10% of the sources are spurious, for $I \sim 13$ approximately 20% are spurious, and for $I \sim 14$ more than 30% are spurious.

With a pixel radius of $\sim 15''$, we would expect to achieve better than $1''$ precision in our astrometry. The fact that we require a $10''$ matching radius is somewhat surprising. Indeed, in performing the magnitude zero-point calibration 90% of the matches to *Hipparcos* were better than $1''$. The *Hipparcos* stars were bright ($I < 10$), and we find that for our match to 2MASS we match to better than $1''$ for most of the bright stars. It seems likely that there is a systematic error that affects the astrometry at the faint end.

4. SELECTION OF VARIABLES

4.1. Rescaling ISIS Errors

Before proceeding with the selection of variables, it is useful to rescale the formal flux errors from ISIS to match the empirically observed errors. This is necessary since the formal errors are assumed to represent the real errors when used by variability tests such as Stetson’s “ J ” (Stetson 1996). We follow a procedure similar to that used by Kaluzny et al. (1998).

To do this we calculate the reduced χ^2

$$\chi^2/N_{\text{dof}} = \frac{1}{N-1} \sum_{i=1}^N \left(\frac{I_i - \bar{I}}{\sigma_i} \right)^2 \quad (1)$$

for every light curve and plot it as a function of I (Fig. 4). Here I_i is the measured magnitude at time i , \bar{I} is the mean magnitude for the light curve, and σ_i is the formal error assigned to the magnitude measurement. The observed χ^2/N_{dof} rises well above the expected value of 1 at the bright end. This is because systematic errors dominate the light curves of the bright stars, as described in § 3.3. To account for these systematics in our errors, we fit a curve to the “ridge” of the observed χ^2/N_{dof} versus I distribution. We then multiply the formal errors by the square root of this function. The resulting “corrected” χ^2/N_{dof} versus I is shown in Figure 4b.

4.2. Stetson’s Variability Index

As a preliminary selection of variable stars, we apply the Stetson “ J ” variability test (Stetson 1996). To apply this statistic, one forms n pairs of observations each with a weight w_k and then calculates

$$J_S = \frac{\sum_{k=1}^n w_k \operatorname{sgn}(P_k) \sqrt{|P_k|}}{\sum_{k=1}^n w_k}, \quad (2)$$

where

$$P_k = \begin{cases} \delta_{i(k)} \delta_{j(k)}, & \text{if } i(k) \neq j(k), \\ \delta_{i(k)}^2 - 1, & \text{if } i(k) = j(k), \end{cases}$$

is the product of the normalized magnitude residuals,

$$\delta = \sqrt{\frac{n}{n-1} \frac{I - \bar{I}}{\sigma_i}},$$

of the two paired observations. The pairing and weighting scheme that we use is analogous to that employed by Kaluzny et al. (1998). We use a timescale of 30 minutes for pairing, assigning a weight of 1.0 to pairs formed by distinct points and a weight of 0.1 to “pairs” formed from a single point.

To select the variable stars we apply a cut of $J_S > 1.0$ (Fig. 5). This selects 2830 light curves, all of which show some form of correlated variability.

4.3. Selection of LPVs

The majority of light curves selected with the above procedure do not show any periodicity within the 30 day window of observations. Typically these light curves increase or decrease monotonically over the run, although there are some that achieve a minimum or maximum magnitude. For the purposes of this paper, we define a “long-period variable” (LPV) to be any variable for which the fit to a parabola is substantially better than the fit to the mean. These are most likely Mira variables or semiregular or irregular variables.

To separate the LPVs from the other variable stars, we apply the following simple cut: We first fit a parabola to all the light curves flagged as variable by the J_S cut. We then calculate the reduced chi-square, χ^2/N_{dof} (we use the shorthand $\chi^2_{N_{\text{dof}}}$, e.g., χ^2_{N-3} in the case of fitting to a parabola), for each fit. True LPVs will show dramatic improvement when fitted with a

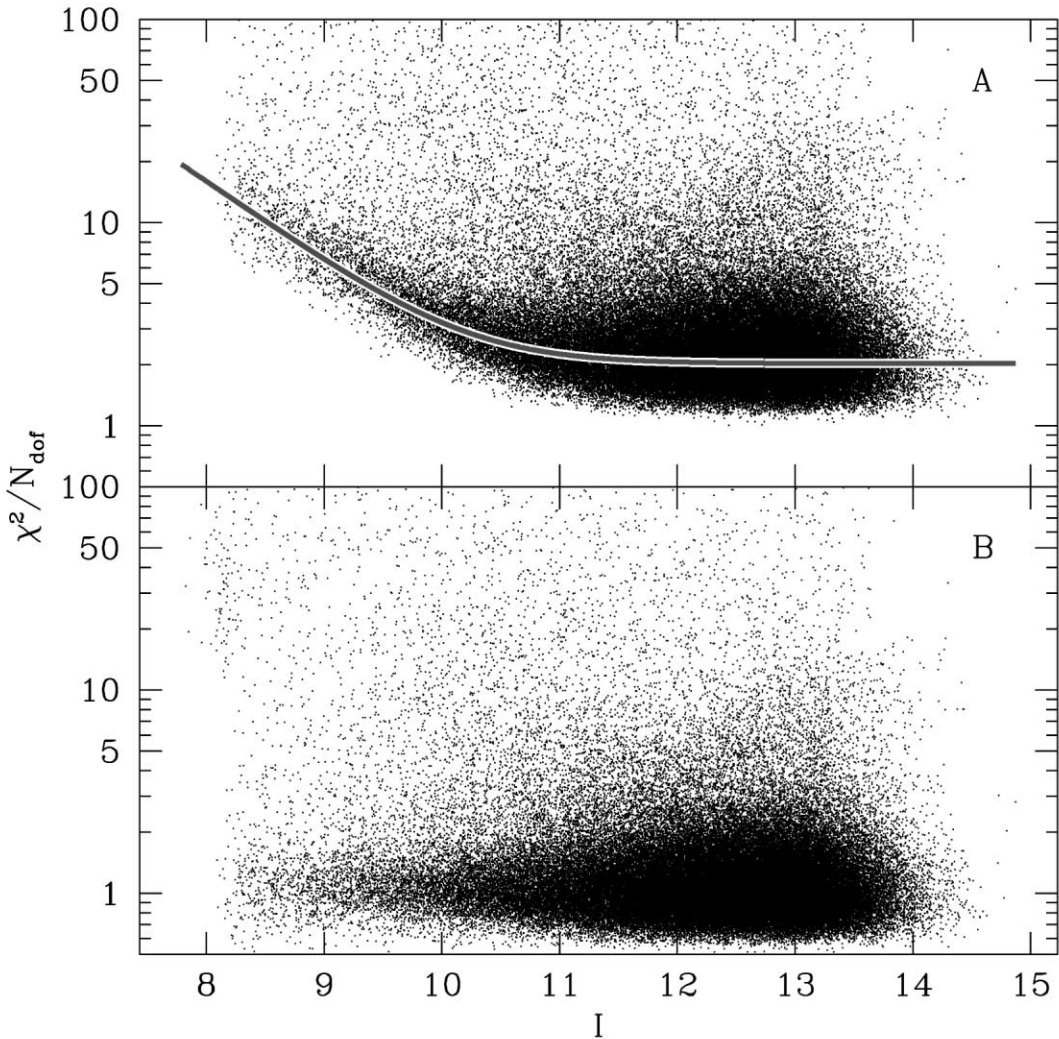


FIG. 4.—(a) Reduced χ^2 of 98,000 light curves vs. I magnitude of the objects on the reference frame. The line shows the function used to rescale the formal photometric errors from ISIS. (b) Reduced χ^2 vs. I following correction of formal flux errors from ISIS (§ 4.1).

parabola as opposed to fitting with the mean (χ^2_{N-1}). To select the LPVs we perform an F -test, classifying any light curve with $\chi^2_{N-3}/\chi^2_{N-1} < 0.4$ as an LPV (Fig. 6). This procedure selects 1535 candidate LPVs, leaving 1295 candidate non-LPV variables.

We chose this cut empirically at a point where light curves that may be best fitted with a third-order polynomial begin to be mixed in with the parabolic light curves. An example of how a light curve with $\chi^2_{N-3}/\chi^2_{N-1} \ll 0.4$ compares with a light curve with $\chi^2_{N-3}/\chi^2_{N-1} \lesssim 0.4$ is shown in the inset of Figure 6.

4.4. Removal of Spurious Variables

In § 3.3, we claimed that our systematic errors are uncorrelated on timescales longer than 20 minutes. Although this is true for the majority of stars, we do see a number of light curves that show nearly identical variations. These trends can be classified into three basic types: “template 1” like (Fig. 7a), “template 2” like (Fig. 7b), and “template 3” like (Fig. 7c). Since image subtraction assumes conservation of flux, there are a number of light curves that show the same trends, but reflected about the horizontal axis.

Regardless of the nature of these systematic variations, we believe the most straightforward way to reject light curves that

show these trends is to reject those that have a substantially smaller χ^2 when fitted, point-by-point, to the template light curves, than when fitted to the mean. When fitting to the templates we allow one free parameter: an overall scaling of the variations above and below the mean. We apply different cuts for the LPV and non-LPV light curves, since a very strict cut tends to reject more LPVs than non-LPVs, particularly for fitting to template 1. For template 3, we also imposed a magnitude cut to avoid removing variables that had a numerically good fit but had a maximum at a different time and were thus probably not spurious. Looking back through the permitted LPVs, we rejected four candidates by eye that showed a strong resemblance to template 3 or template 2. The template 3 cut was applied after all other cleaning steps. We also observed a number of light curves that appeared to be correlated with the air mass of the observations. These tended to be removed more efficiently by fitting to template 1 or template 2 than by defining a separate template, as a number of “true” variables showed small 1 day oscillations on top of an overall “real” variation and would be rejected by a separate template.

As a check on our template 3 rejections, we examined the light curves released by the Northern Sky Variability Survey (NSVS; Woźniak et al. 2004) for the 13 objects rejected by template 3. The survey made use of the Robotic Optical

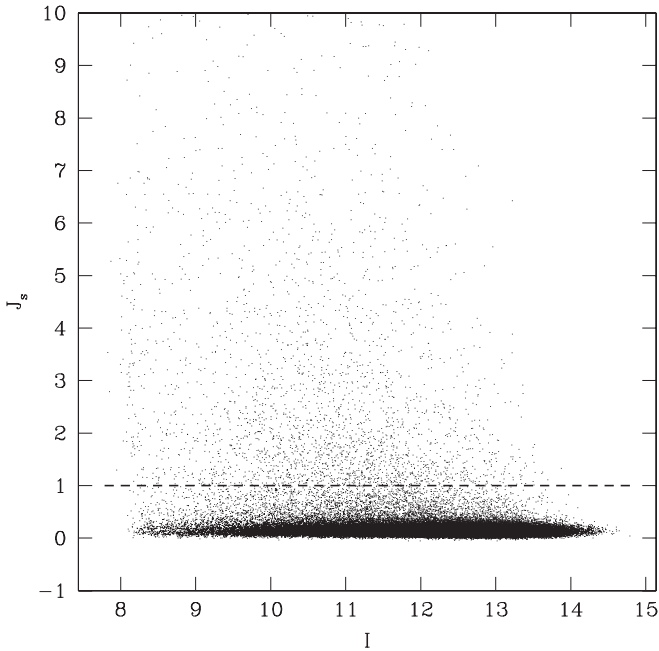


FIG. 5.—Plot of Stetson’s “*J*” variability index (J_S) vs. *I* magnitude. The 2830 objects lying above the dashed line ($J_S = 1.0$) were selected as candidate variable stars (§ 4.2).

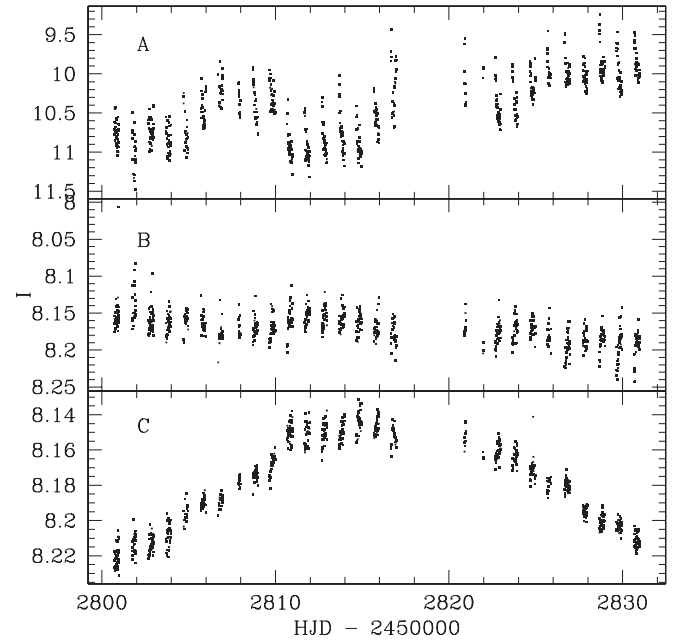


FIG. 7.—Light curves used as templates to remove spurious variables (§ 4.4).

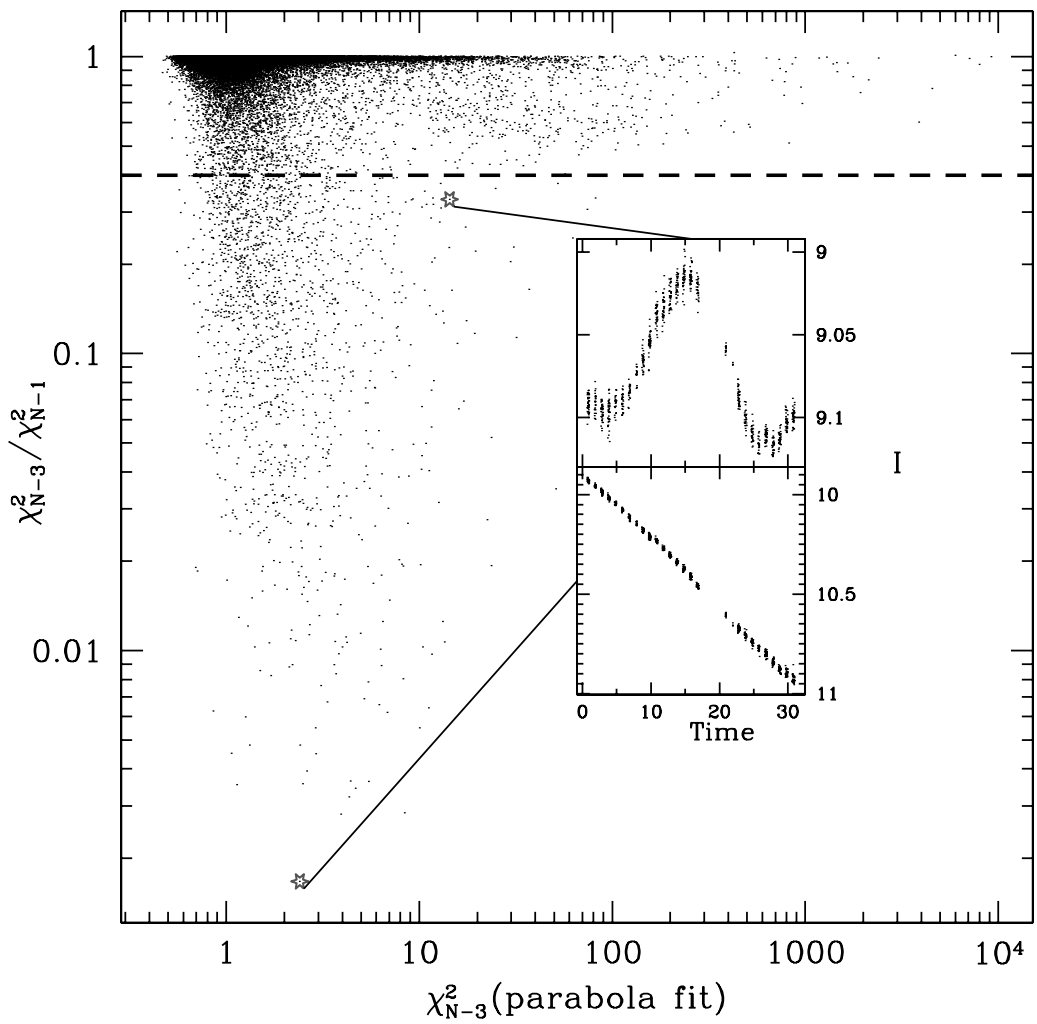


FIG. 6.—Ratio of reduced χ^2 for fit of a parabola to χ^2 about the mean (χ^2_{N-3}/χ^2_0) vs. reduced χ^2 for fit of parabola χ^2_2 . This plot is for all 98,000 light curves. The 1535 objects below the dashed line ($\chi^2_{N-3}/\chi^2_0 = 0.4$) that also had $J_S > 1.0$ are light curves that we classified as LPVs (§ 4.3). Inset: Light curves with $\chi^2_{N-3}/\chi^2_0 \ll 0.4$ are better fitted with a parabola than those with $\chi^2_{N-3}/\chi^2_0 \lesssim 0.4$.

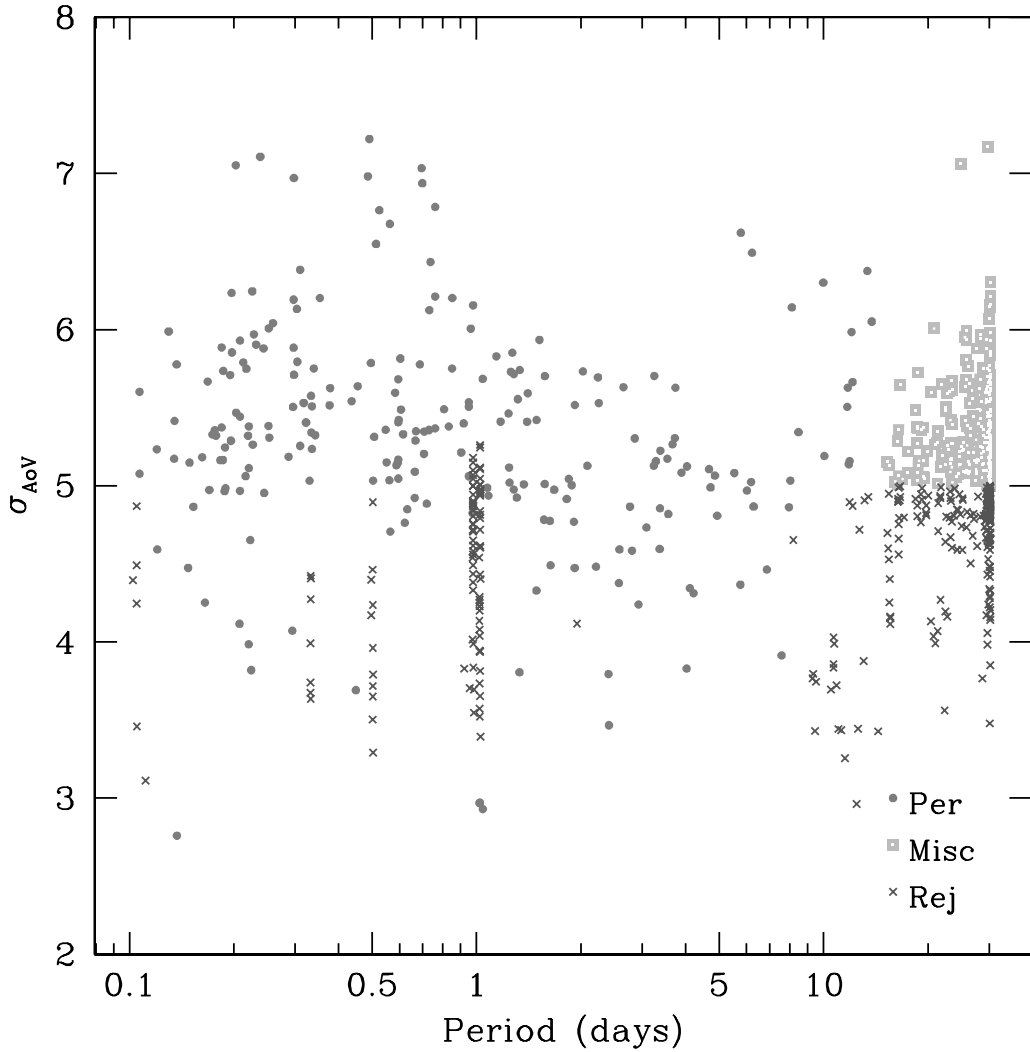


FIG. 8.—Period vs. σ_{AoV} for the remaining 791 non-LPV variables. The quantity σ_{AoV} is the measure of confidence assigned to the period fit (see § 4.5). The circles show the 231 objects classified as “periodic,” the squares are the 266 objects classified as “miscellaneous,” and the crosses are the 294 rejected light curves. Periodic light curves have periods less than 14 days and do not (except in a few cases) have periods near a harmonic of 1 day. Miscellaneous light curves have $P > 14$ days and $\sigma_{\text{AoV}} > 5$.

Transient Search Experiment (ROTSE-I) to provide to the public a temporal record of the northern sky over the optical magnitude range from 8 to 15.5. Notably, the optics and CCD used for this telescope are now in use on the HAT-5 instrument. The majority of our template 3-like light curves have a full amplitude of ~ 0.05 mag, however, as they are classified as LPVs, one might expect that if they are real then a number of them should have full amplitudes greater than ~ 0.1 mag when observed over a longer baseline. The typical rms for the NSVS light curves of these objects is 0.05 mag, so any variations with full amplitude less than ~ 0.1 mag would be unrecognizable in these light curves. We find that three of the template 3-like light curves appear to show variations in the NSVS. These three, which include HAT 199-648, HAT 199-3997, and HAT 199-4205, will remain in our catalog. It should be noted that all three of these light curves show an inverted template 3-like shape, and that all three of them have full amplitudes greater than 0.1 mag in our observations and are therefore already suspect as template 3-like.

For the variables classified as LPVs, we reject nine light curves with $\chi^2_{\text{temp1}}/\chi^2_{N-1} < 0.35$, 10 light curves with both $\chi^2_{\text{temp3}}/\chi^2_{N-1} < 0.23$ and $I_{\text{ref}} < 10.0$, and an additional four by eye. For non-LPVs we reject 359 light curves

with $\chi^2_{\text{temp1}}/\chi^2_{N-1} < 0.6$ and another 99 light curves with $\chi^2_{\text{temp2}}/\chi^2_{N-1} < 0.85$.

As a further cleaning step, we also rejected 46 of the non-LPV light curves that had fewer than 693 points. We did not reject two light curves that had fewer than 693 points but appeared to show real variability.

4.5. Selection of Periodic Variables

To search the remaining 791 candidate non-LPV variable stars for periodicity, we use a variation of the period-finding algorithm by Schwarzenberg-Czerny (1996). This algorithm is implemented in a code due to J. Devor (2004, private communication). The code provides the two “optimal” periods, along with a measure of confidence for these periods (σ_{AoV}).

Using the best period as a starting point, we proceeded to classify the remaining 791 non-LPV light curves by hand as either periodic (with period less than 14 days), miscellaneous (a light curve that is not an LPV and does not have a period under 14 days), or a light curve to reject (typically, light curves that appeared to be dominated by periods that were harmonics of 1 day, or light curves that resembled the trends of § 4.4). We chose a 14 day cutoff for the period to ensure that any light

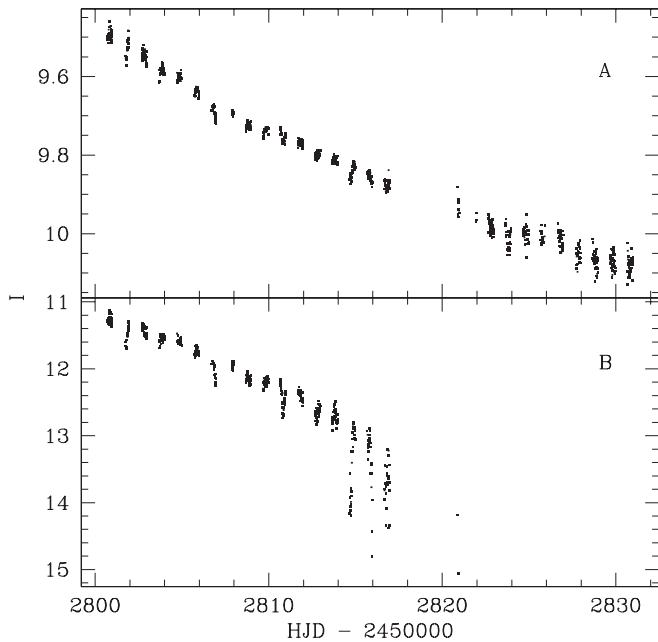


FIG. 9.—(a) LPV matched to V484 Cyg, an EA/SD binary, as well as to V1360 Cyg, a Mira variable. The eclipses are less pronounced than in (b), meaning that this light curve likely corresponds to the Mira V1360 Cyg. (b) Light curve of an object within 2 pixels of (a). This light curve shows deeper eclipses than (a) and is likely V484 Cyg. The larger flux variations due to (a) are blended into this light curve. V484 Cyg is not included in the catalog of variables.

curve we classified as periodic completed more than two full periods within the window of observations. Since rejecting light curves by eye is a highly subjective procedure, we decided to find objective cuts that would generally yield the same subjective classifications. We rejected light curves whose best period fell near a harmonic of 1 day and had a low value of σ_{AoV} , and light curves with a best period greater than 8 days and $\sigma_{\text{AoV}} < 5$. For the remaining light curves, we called the object “periodic” if the best period was less than 14 days, and “miscellaneous” if not. These particular cuts were chosen empirically as providing the cleanest removal of “suspicious” light curves. The results of these cuts are shown in Figure 8. We looked through the rejected light curves and rescued eight cases that we believed were clearly variables. We also looked through the periodic and miscellaneous light curves, rejecting five light curves that showed a significant resemblance to

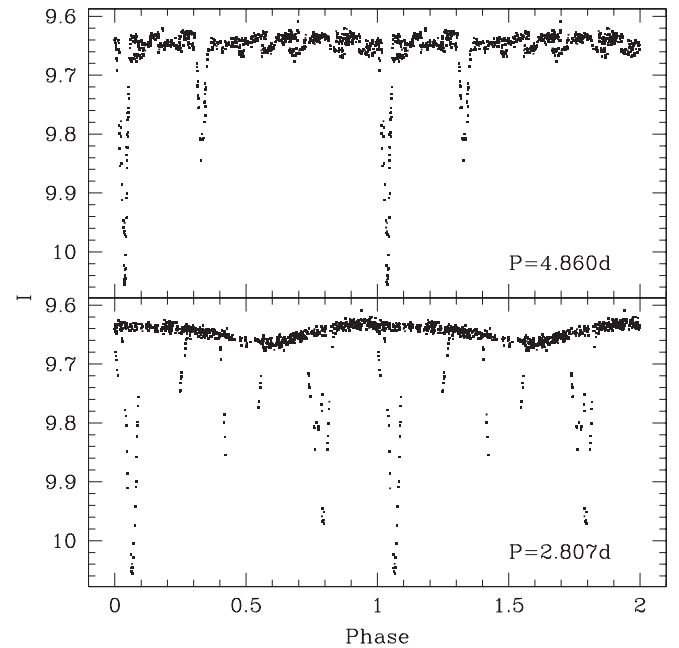


FIG. 10.—Phase-folded light curve of HD 227269, showing eclipses with a period of 4.860 days and pulsations with a period of 2.807 days. The system may be a blend between two distinct variables separated by $\sim 9''$ (§ 5.1).

one of the templates (§ 4.4). There were 294 light curves rejected in this step. We erred on the side of caution for the rejection cuts; a look through the rejected light curves reveals many other probable “true” variables. For this reason, we do not claim completeness for our periodic or miscellaneous-class variables.

4.6. Blending

Following the above classification and cleaning procedures, and prior to the removal of the template 3-like light curves, we were left with three sets of variable stars: 1526 LPVs, 266 miscellaneous variables, and 231 periodic variables. However, as mentioned in § 3.2, one shortcoming of the ISIS photometry program “phot.csh” is that it does not account for blending in the subtracted images. Although true variables are generally well separated in the subtracted images, any given variable may have a number of nonvariable stars within a `rad_aper`. As a result, “phot.csh” will sample a portion of the variable flux from the nearby variable star when measuring the magnitude

TABLE 1
HAT CATALOG OF “KEPLER FIELD” VARIABLES

ID (HAT 199-)	α (J2000)	δ (J2000)	I	J	H	K	2MASS ID	Class.	I_{\min}	I_{\max}	P (days)	GCVS ID	GCVS Class.
00001.....	19 44 49.29	37 32 59.6	7.787	5.601	4.760	4.251	1275.128417	LPV	7.987	7.642
00006.....	19 40 59.04	36 43 32.8	7.959	4.039	2.999	2.461	1267.127829	LPV	8.284	7.800	...	V942 Cyg	M
00009.....	19 46 42.35	34 50 40.6	7.989	5.097	4.212	3.875	1267.127829	LPV	8.024	7.917
00020.....	20 03 57.48	39 59 16.7	8.063	5.494	4.491	4.093	1299.142572	LPV	8.116	8.003	...	V423 Cyg	SRA
00029.....	20 01 50.00	33 28 24.0	8.090	LPV	8.172	8.052
00049.....	19 43 09.81	34 06 09.6	8.137	6.050	5.146	4.785	1241.138907	LPV	8.294	8.028
00060.....	19 25 08.27	35 59 57.9	8.151	8.142	8.171	8.154	1259.119674	Ecl.	8.275	8.044	1.4891	V556 Lyr	...
00061.....	19 41 17.60	40 10 41.9	8.154	6.758	5.819	5.538	1301.125923	Misc.	8.179	8.124
00074.....	19 49 59.62	35 40 14.5	8.173	7.833	7.700	7.627	1256.139193	Puls.	8.192	8.153	0.1650

NOTES.—Units of right ascension are hours, minutes, and seconds, and units of declination are degrees, arcminutes, and arcseconds. Coordinates are from 2MASS where available, as are J , H , and K measurements. The maximum and minimum I are the sixth from the brightest and dimmest measurements, respectively. Table 1 is presented in its entirety in the electronic edition of the Astronomical Journal. A portion is shown here for guidance regarding its form and content.

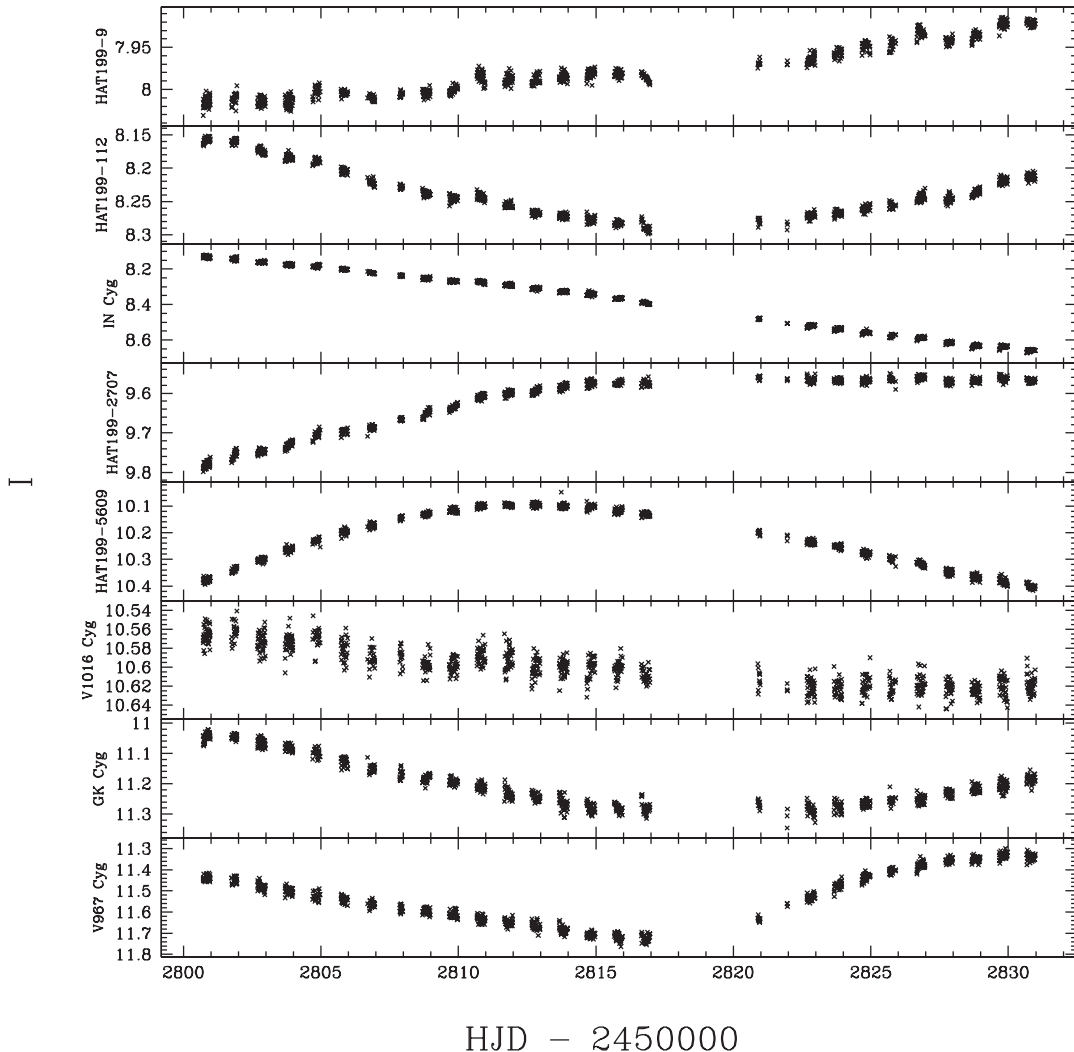


FIG. 11.—The *I*-band light curves of eight LPVs in our catalog. A few of the variables that matched with the GCVS include V1016 Cyg, a symbiotic nova, and GK Cyg and V967 Cyg, which are RV Tauri variables.

of the nonvariable star, and our procedure may flag some of these stars as variables. Existing routines, such as DAOPHOT, that perform “deblending” profile photometry do not allow for negative fluxes and, as such, will not work on subtracted images. Moreover, running these routines on the absolute value of the subtracted images will have difficulty dealing with the case of two nearby variables, with one a positive variation and the other a negative variation. Since “phot.csh” weights each pixel in the aperture by the PSF, it will measure less flux for the nonvariable stars than for the true variables, as the nonvariables will be off-center from the variable flux. This suggests a method to separate the true variables from the blended light curves.

The first step is to identify blending groups. From each blending group, we identify the true variable as the light curve that has the highest standard deviation (in flux). To select the blending groups, we first find all pairs of variable stars that are separated by fewer than 6 pixels. There are a total of 461 pairs (well above the expected number due to random matching), involving 695 distinct light curves. We then form groups so that pairs such as 1-2 and 2-3 will be grouped into 1-2-3, etc. The largest groups contained five light curves (there were three of these groups). This formed 305 groups, so that 390 objects were rejected as blended light curves. Two of the remaining

periodic variables were then removed by hand, as they showed no obvious periodicity and a strong likeness to template 1.

Following the correction for blending (and removal of template 3-like LPVs as per § 4.4), we arrived at our final list of variables, consisting of 1169 LPVs, 241 miscellaneous variables, and 207 periodic variables, for a total of 1617 distinct variables. The periodic variables were then classified, by hand, into two general classes: eclipsing variables (157 objects) and pulsating variables (50 objects). These further classifications are subjective and represent the authors’ suspicions as to whether or not the light curve appears to show some form of eclipses.

Because we only choose one true variable from each blending group, we will reject true variables that lie within 6 pixels of other, larger amplitude (in flux), true variables. When two true variables are nearby one another, the light curves of both objects will likely show variability blending. Our procedure will reject the true variable, whose flux light curve has a smaller standard deviation. However, the light curve of the accepted variable will likely show some variations due to the rejected variable. For 1617 variables randomly distributed across the image, we expect ~ 70 such pairings, or roughly 4% of all cases. Since we are more inclined toward correctly identifying variables than forming a complete list

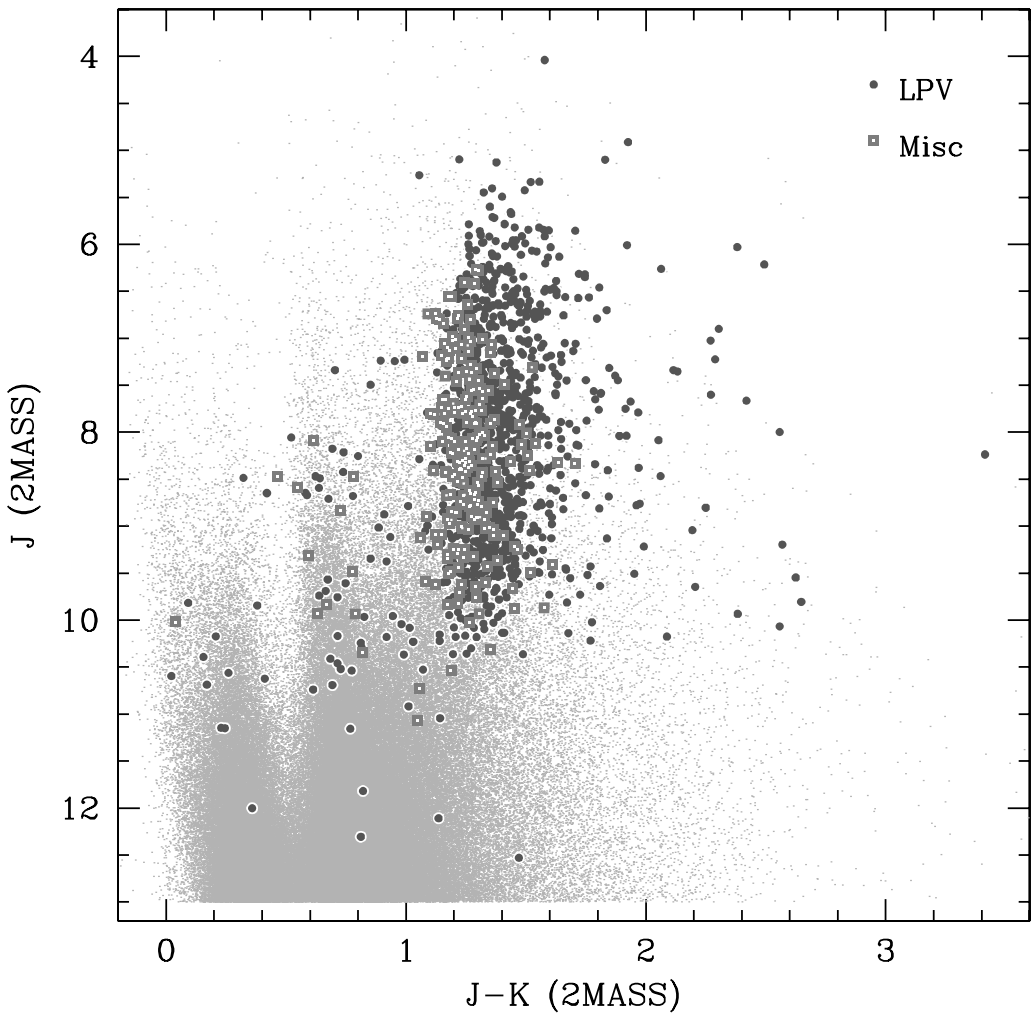


FIG. 12.— J vs. $J-K$ CMD showing the location of LPVs and miscellaneous variables relative to all 2MASS objects in our field with $J < 13$. Magnitudes are taken from 2MASS. LPVs are shown as circles and miscellaneous variables as squares, and the general population of objects is shown in gray. Note that both the LPVs and the miscellaneous variables are generally redder than the overall population, with LPVs typically being redder than miscellaneous variables. LPVs are mainly Mira variables, while miscellaneous may include many type I and type II Cepheids that have periods between 14 and 30 days. The bluest miscellaneous variable, with $J = 10.02$ and $J-K = 0.039$, is V1920 Cyg, a PV Telescopii type variable (§ 5.4).

(that will include many false positives), we choose to live with the rejections. It should be noted, however, that as many as 4% of our variable-star light curves may show contamination from another nearby variable star that is not included in the list. This number may be even higher if there is clustering, as suggested in § 3.4.

As an example of this variability blending, consider Figure 9. Figure 9a shows the light curve of an object that we matched with V484 Cyg, an EA/SD binary with eclipses of 1 mag in V (between 13.5 and 14.5) and a period of 1.29 days, as well as to V1360 Cyg, a known Mira variable. Our observations reveal a monotonic decrease in flux from $I = 9.48$ to $I = 10.11$ over 30 days, with slight eclipses. A search of nearby objects revealed a star within 2 pixels with a light curve that showed deeper eclipses on top of an overall declining envelope (Fig. 9b). Indeed, both these objects are matched to separate 2MASS objects. This, we believe, is an especially pronounced case of variability blending in which two real variables lie within each others' aperture and, hence, the variability is blended into both objects. In this case Figure 9b likely corresponds to V484 Cyg, and Figure 9a to V1360 Cyg. Our selection method retained V1360 Cyg while rejecting V484 Cyg as a blended light curve. Because the light curve of V484 Cyg

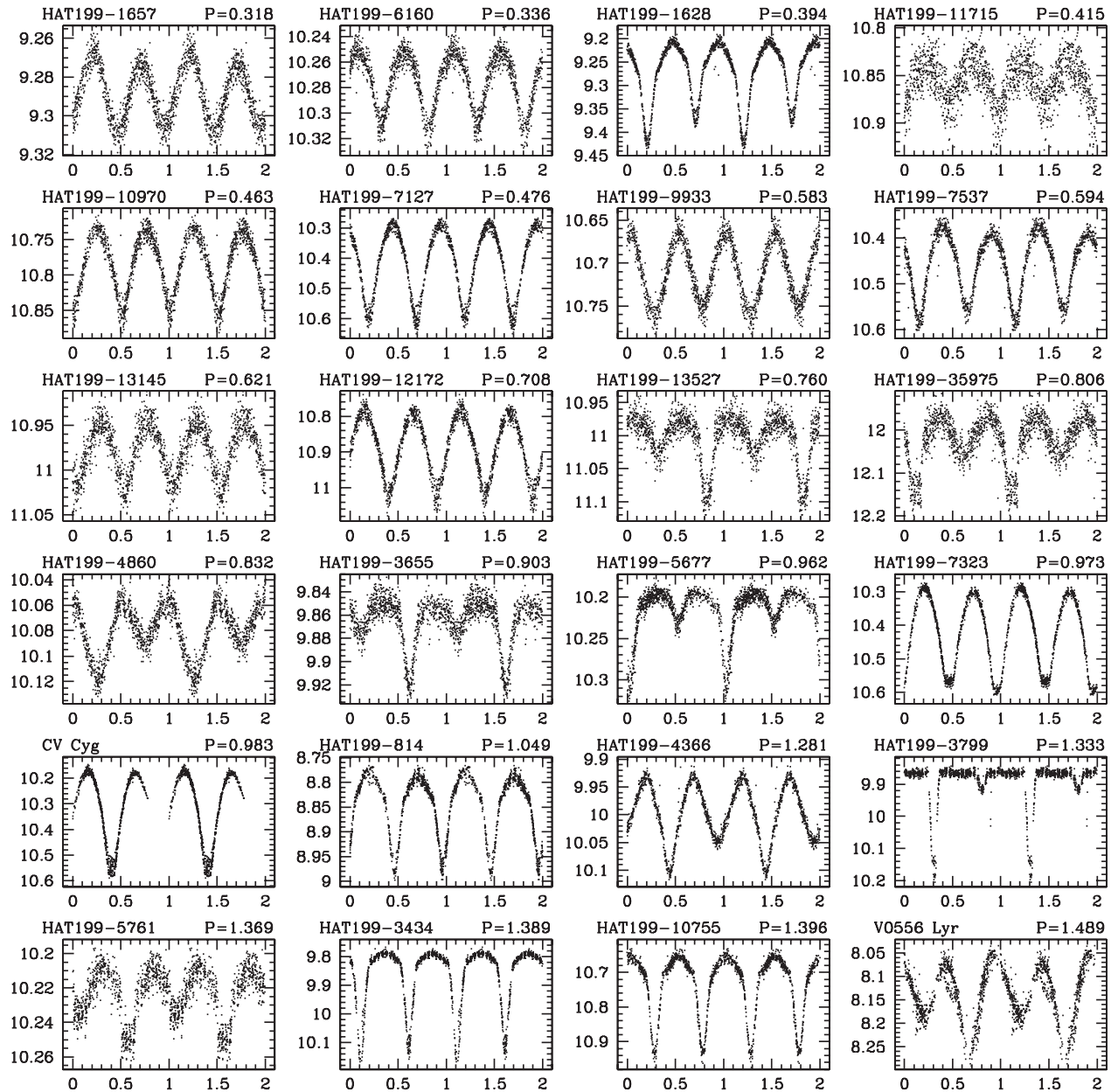
is strongly corrupted by the presence of the nearby LPV, we will not attempt to “rescue” it into the catalog and will include only V1360 Cyg.

It is important to stress that in this procedure we do not in any way correct for the blending that results from resolution limits, whereby a number of distinct sources are blended into an individual object. Indeed, many of the individual light curves may consist of the summed light from several sources lying along the same line of sight. Instead, the blending that we correct for is the blending of variability into multiple resolved objects that results from “phot.csh” applying simple weighted aperture photometry on the subtracted images.

5. CATALOG OF VARIABLES

The full catalog of variable stars, including 2MASS coordinates and IDs where available, is presented in Table 1. The catalog and light curves are also available on the World Wide Web.⁴ In the table, we provide the HAT ID for each object, which uses the form HAT199-xxxxx, where the number is between 00001 and 98000 and sorts the light curves by reference

⁴ See <http://cfa-www.harvard.edu/~gbakos/HAT/LC/199/>.



Phase

FIG. 13.—The I -band light curves, sorted by period (given in days), for 48 of the 157 EBs in our catalog. GCVS names are provided where available.

magnitude. In this section, we discuss the overall properties of the various classes of variables, as well as some of the interesting cases from each class.

5.1. Matching to Known Variables

To cross-check with known sources, we matched our list of variables to the Combined General Catalogue of Variable Stars (GCVS; Kholopov et al. 1998). The GCVS contains 334 objects in our field; we obtained matches to 159 of these using a $30''$ matching radius. As mentioned above, one of our sources matched to two independent GCVS sources, so that only 158 of our sources were classified in the GCVS. To match we used 2MASS coordinates for our objects where available. There are 82 matches that lie within $5''$. We take a liberal matching radius of $30''$ to allow for matches to variables that

do not have 2MASS coordinates, as well as to allow for the possibility that some of our variables are matched to the incorrect 2MASS counterpart. We also note that the positions in the GCVS may come from a wide variety of epochs, further necessitating the liberal matching radius.

Of the 176 GCVS variables that do not match with one of our variables, 111 have $V > 13.5$ and are thus likely to be either too faint to detect as stars or so faint that the variations are lost in the background noise in our observations. There are 24 unmatched variables with $V < 10$ that appear to be correlated with saturated stars in our I -band observations. Of the remaining 40, there are nine eclipsing binaries, seven of which are Algol-like (EA) and could go undetected if none of the eclipses are observed, or if only small portions of a few eclipses are observed. There are eight Mira variables for which

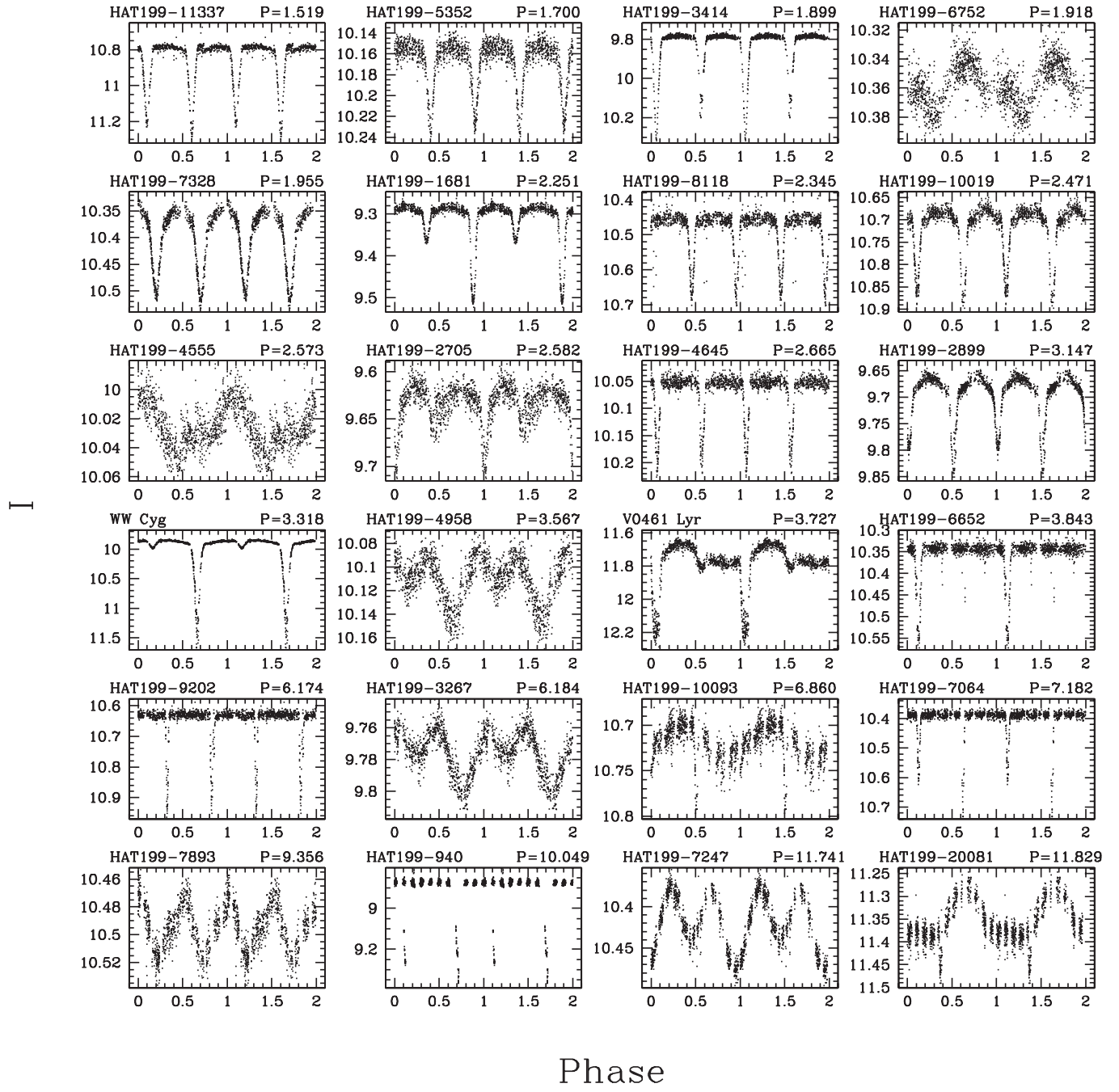


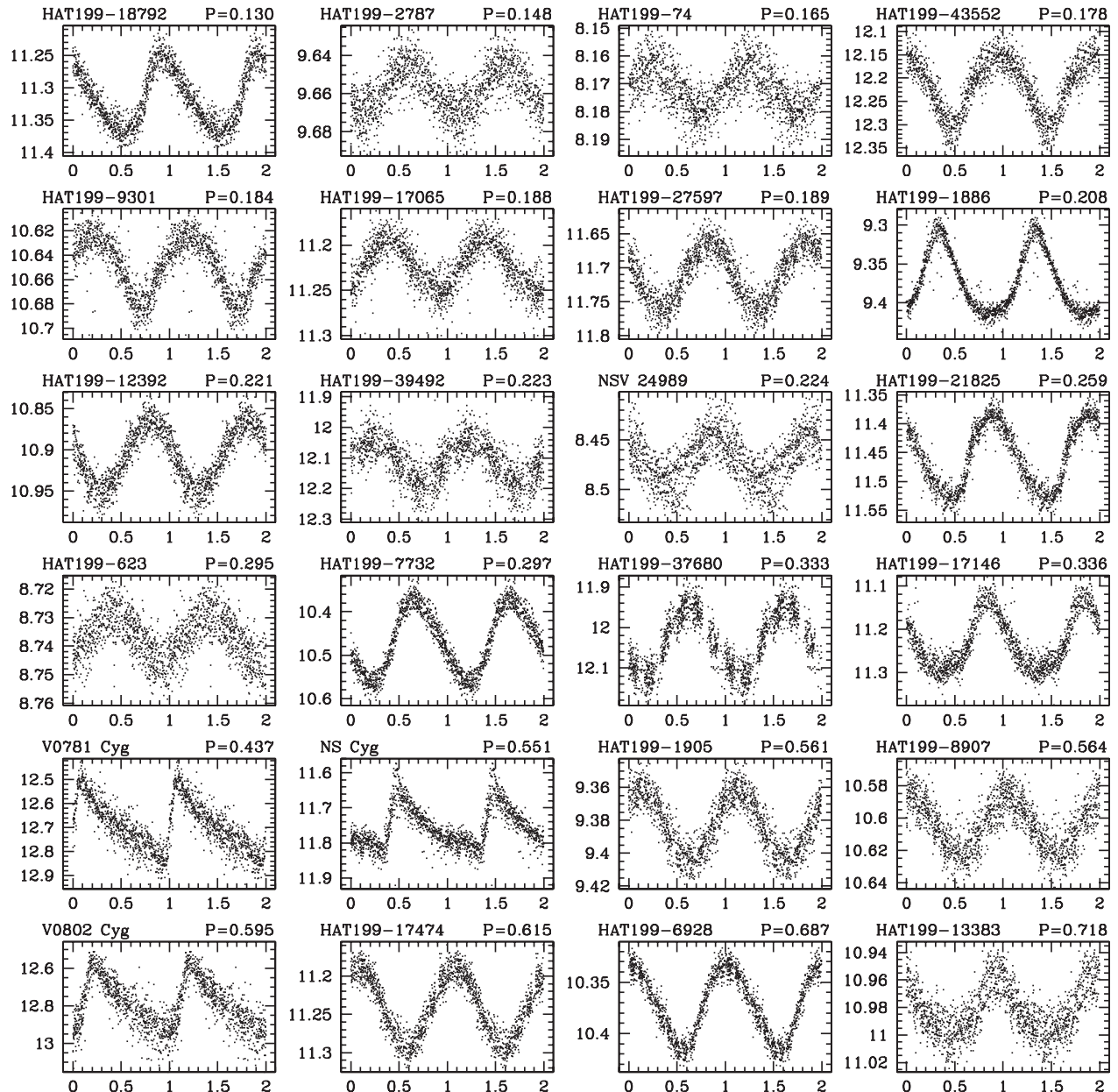
FIG. 13.—Continued

the change in magnitude over 30 days may have been too small to detect. Of these eight, the five that have ephemerides available in the GCVS appear to have been too dim to detect during the observations or varied by an amount less than 10σ above the noise. There are 19 semiregular and slow irregular variables, all of which may have varied only slightly over the course of our observation. Finally, we can expect about five GCVS variables to be excluded from the catalog because of variability blending. We see that we can account for all the GCVS variables in our field to which we did not obtain matches.

We also matched our catalog to the New Catalogue of Suspected Variable Stars, including the supplemental series (NSV; Kukarkin et al. 1982). Using the same matching radius as

above, we obtained matches to 20 sources. The NSV designation for these confirmed variables is provided in our catalog.

There have also been some more recent searches for variability in fields overlapping this one. Notably, Alonso et al. (2003), as part of the STARE project, found that over 40 of the $\sim 14,000$ stars observed in their “Cyg0” field had pulsation periods between 5 and 40 days. Of these, they identify HD 227269 as a highly eccentric eclipsing binary showing possible pulsations. We do detect HD 227269 as an eclipsing binary and also see the same pulsations (Fig. 10). Alonso et al. mention, however, that a Digitized Sky Survey image of the star reveals a companion that is similar in brightness within $\sim 9''$. At this separation the stars would be blended in our observations, and it is possible that the pulsations are not occurring



Phase

FIG. 14.—The *I*-band light curves, sorted by period (given in days), for 48 of the 50 pulsating variables in our catalog. The other two are shown in Fig. 17.

in the binary system, though this system does merit further investigation.

Another transit search that we overlap with is the Vulcan Photometer project, which has found over 50 eclipsing binaries out of 6000 stars observed (Borucki et al. 2001). Of the brightest 6000 stars we observed, 24 were eclipsing binaries. However, because our brightest stars may contain many more blended objects than the 6000 relatively isolated stars observed by Vulcan, these two populations may not be directly comparable. The differences in the detection rates may also be partially explained by differences in classifications. We should also note that the Vulcan binaries include many low-amplitude systems, which may not have $J_S > 1$ and hence would not be flagged as “large amplitude” variables by our method.

In § 4.4, we made use of the NSVS light-curve database (Woźniak et al. 2004) to manually check the rejected template 3-like light curves to determine whether any showed variability in an independent experiment. It may be useful in the future to also compare our entire catalog of variables with the NSVS database; however, that is beyond the scope of this paper.

5.2. Long-Period Variables

As mentioned in § 4.3, we cataloged any object whose light curve was well fitted by a second-order polynomial as an LPV. We identified 1169 LPVs, of which 1026 are newly discovered variables. Of the known variables, 19 are newly confirmed NSV sources. Figure 11 shows a few of the interesting cases.

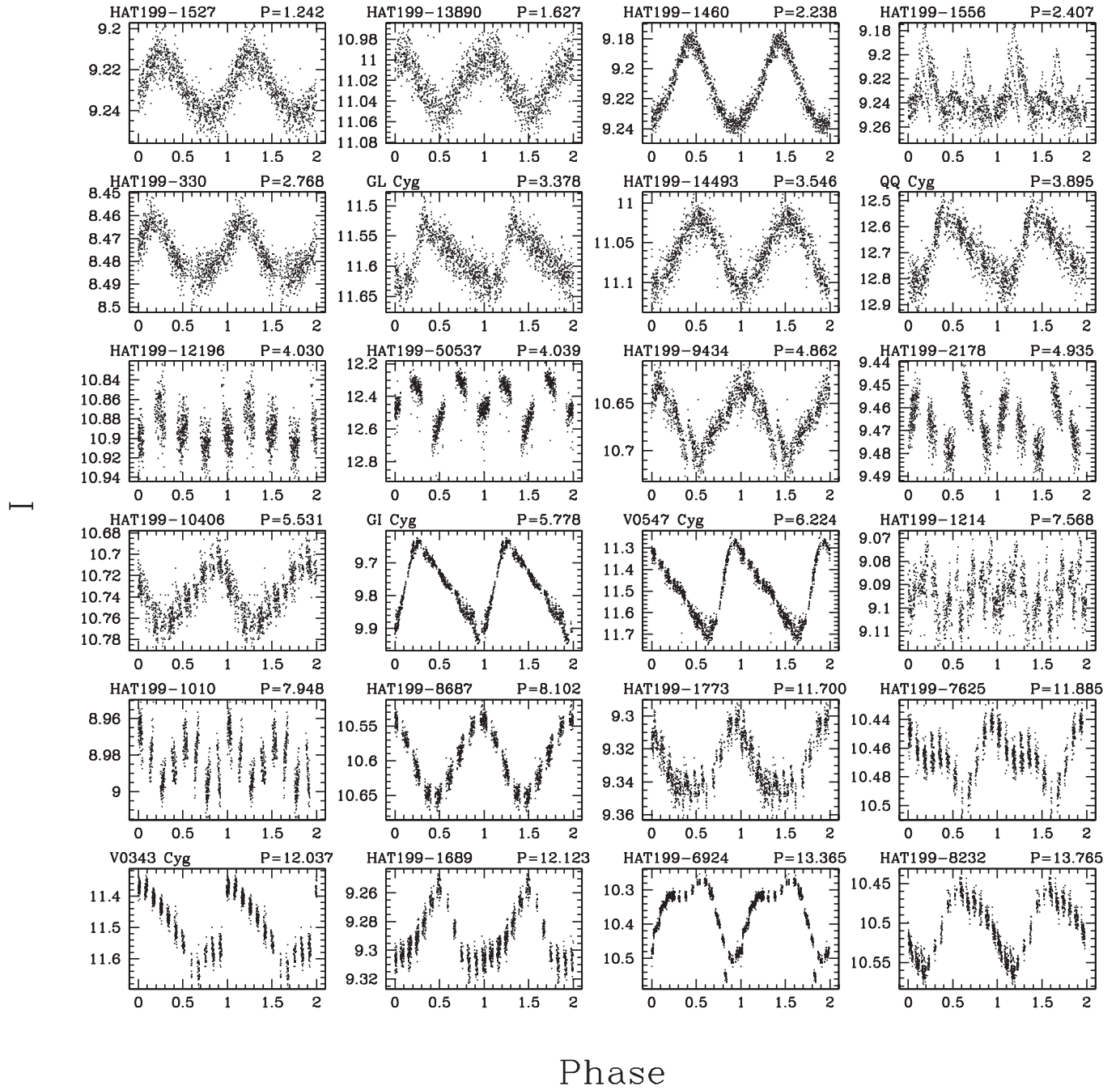


FIG. 14.—Continued

The majority of the LPVs are likely to be Mira variables, which all have periods longer than our 30 day window. Indeed, 77 of the 97 matched LPVs are known Miras. Recently there has been a great deal of interest in pinning down the various period-luminosity relations for Mira variables observed by the microlensing surveys (e.g., Wood et al. 1999; Wood 2000; most recently, Groenewegen 2004). All these have used observations of the Large and Small Magellanic Clouds, where the distances can be factored out of the relations. Because we cannot assume a uniform distance for our observations, this population of Miras will likely be less useful toward this endeavor. Our population, however, is substantially brighter and hence may be more useful for detailed investigations of asymptotic giant branch stars.

Figure 12 shows the location of the LPVs on a J versus $J-K$ color-magnitude diagram (CMD). The infrared magnitudes J and K are taken from the match to 2MASS. As expected, the LPVs are generally redder than the majority of stars and tend to lie along the giant branch of the CMD.

Among the more exotic variables that we classify as LPVs are V1016 Cyg, a well-studied symbiotic nova whose cool component is a $P = 474$ day Mira variable (see, e.g., Parimucha 2003), and a few RV Tauri stars, including GK Cyg and V967 Cyg.

5.3. Periodic Variables

We identified 207 large-amplitude (full amplitude greater than 0.032 mag) variables that show periods less than 14 days;

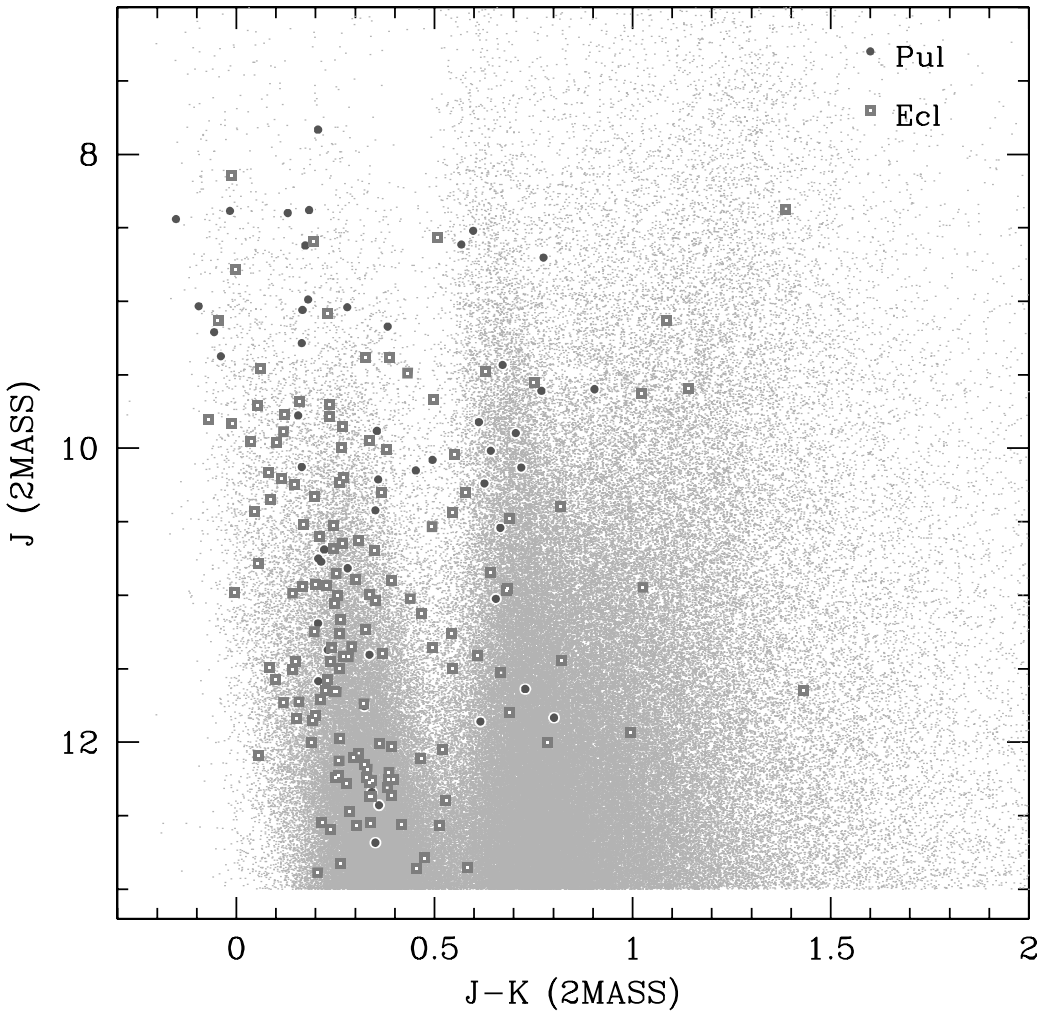


FIG. 15.— J vs. $J-K$ CMD showing the location of EB and pulsating variables relative to all the 2MASS objects in our field with $J < 13$. Magnitudes are taken from 2MASS. Note that the axis ranges are not the same as in Fig. 12. Pulsating variables are shown as circles and EBs as squares, and the general population of objects is shown in gray. Note that both classes of periodic variables tend to lie toward the blue end (on the main sequence) relative to the LPVs and miscellaneous variables (Fig. 12).

180 of these are newly discovered. As discussed in § 4.5, this cutoff at 14 days was to ensure that any star classified as periodic had been observed for two full periods. We further classified the periodic light curves into 157 eclipsing binary-like (EB) light curves and 50 pulsating variable-like light curves. Figure 13 shows light curves for 48 of the EBs, and Figure 14 shows 48 of the pulsating variables (the other two pulsating variables are shown in Fig. 17 below).

Of the 30 periodic variables matched to GCVS objects, 11 are Algol-type EBs, three are β Lyrae type EBs, five are W Ursae Majoris type EBs, three are Cepheids, one is a Population II Cepheid, and four are RR Lyrae variables. One short-period (0.224 days) pulsating variable has a match in the NSV. The other known periodic variable that has no counterpart in the GCVS is HD 227269 (see § 5.1).

Figure 15 shows the location of the periodic variables (separated into pulsating and eclipsing categories) on a J versus $J-K$ CMD. Compared with the LPVs and miscellaneous variables (Fig. 12), these objects tend to be blue. For the pulsating stars this is expected, as we are only classifying stars with periods less than 15 days as periodic and the shorter period stars tend to be denser and hotter (e.g., δ Scuti).

The two most studied of the matched objects are WW Cyg, an EA/SD binary, and CV Cyg, a EW/DW binary. Because

WW Cyg shows very deep primary eclipses (3.5 mag in V), it has been frequently observed over the last century. As a result this system has been particularly useful in probing the period changes in close binaries (Zavala et al. 2002). Our observations reveal much shallower eclipses in I (2.05 mag) and clearly reveal the secondary eclipses (0.15 mag in I), which have hitherto been undetected in V . Struve (1946) determined that the primary has spectral type B8, while Yoon et al. (1994) assigned a spectroscopic type of G9 to the secondary. The difference of ~ 1.5 in the amplitude of the primary eclipse in V and I suggests that the secondary should have a later spectral type (later than K3). However, Yoon et al. point out that the photometrically determined spectral types for Algol secondaries are typically later than the spectroscopically determined ones.

CV Cyg is a highly evolved eclipsing system that has been used primarily for the study of period and amplitude changes in close binaries (Demircan et al. 1995). Because the period is nearly 1 day (0.983 days), we do not observe both the primary and secondary eclipses; however, we did obtain approximately 15 observations of minima.

The light curve of one very interesting object that we observe is shown in Figure 16. This object matches the known EA/KE binary V1171 Cyg, discovered by Wachmann (1966).

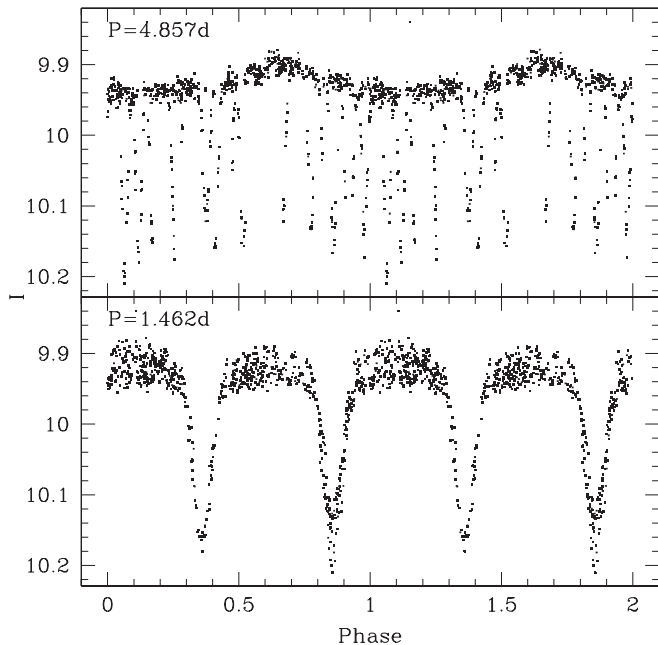


FIG. 16.—Light curve of V1171 Cyg, showing eclipses with an orbital period of 1.462 days and a Cepheid-like upper envelope modulation with a period of 4.857 days (see discussion in § 5.3).

It has also been detected as a visual double with $0''.34$ separation by Couteau (1981). The system has spectral type B9 as listed in SIMBAD. We obtain an orbital period for this system of $P = 1.462$ days, and we also observe an upper envelope modulation with period $P = 4.857$ days and full amplitude ~ 0.05 mag in I . To further analyze this system, we obtained spectroscopy using the FLWO 1.5 m telescope. The spectra show color changes, which indicate that this is not a random blend with another variable more than $1''$ away. The light curve appears to be very similar to that of HD 227269 (§ 5.1 and Fig. 10); however, in this case we have greater confidence that the pulsations and eclipses are occurring in the same system. We suspect that we are looking at a triple system with a Cepheid as one component. Evans et al. (2003) have found that a large fraction of Cepheids exist in triple systems, but they have been unable to determine the masses of all three stars in a given system. If this system is indeed a triple, it may be possible to measure all three masses and thereby add to our picture of the distribution of masses among massive multiple systems (N. Evans 2004, private communication).

We have also observed a number objects that appear to be short-period pulsating stars. These objects have periods between 0.1 and 0.3 days and may well correspond to δ Scuti type variables. A number of these objects show multiple, non-harmonic periods. These include HAT 199-539, which appears to have at least two periods, one at 0.1069 days and another at 0.1198 days, and HAT 199-5178, with periods at 0.1203 and 0.1367 days (Fig. 17).

5.4. Miscellaneous Variables

Variables that were not selected as LPVs and for which the best-fit period was longer than 14 days were classified as miscellaneous. This classification may include a number of periodic variables with periods typically between 14 and 30 days, as well as a number of irregular variables that have timescales shorter than 30 days. We identified 241 such cases, of which all

but four are newly discovered. The four matched cases include V482 Cyg, an R Coronae Borealis star; V1920 Cyg, a PV Telescopii variable; V546 Cyg, an Algol-like eclipsing binary; and V811 Cyg, an SS Cygni type dwarf nova. Light curves of these and other interesting miscellaneous variables are shown in Figure 18.

V482 Cyg is a well-studied member of the rare class of stars known as R Coronae Borealis variables. These carbon-rich variables are noted for their unpredictable and substantial drops in brightness, which are attributed to the formation of soot clouds in the stellar atmosphere. V482 Cyg was in the quiescent state during the observations; however, we do observe a pulsation-like light curve that suggests a period of around 30 days (Fig. 18). This oscillation is very similar to the 39 day period, Cepheid-like pulsations observed in RY Sgr (see, e.g., Lawson & Cottrell 1990).

V1920 Cyg is an extreme helium star that Morrison & Willingale (1987) observed to vary with an amplitude of 0.07 mag in V and a period of 3–4 days. Fadeyev (1990) interpreted these variations as pulsations in the second or higher overtone and used them to constrain the absolute magnitude of the star. Our observations of V1920 Cyg over 30 days reveal irregular variations with no discernible period, but with a timescale of roughly 4 days. We observe a maximum full amplitude of 0.2 mag in I (Fig. 18). This variable is the bluest miscellaneous variable shown in Figure 12.

V811 Cyg is classified in the GCVS as a UGSS-type variable. These stars are dwarf novae that show regular, symmetric outbursts typically lasting 3–10 days. We observed one such outburst for V811 Cyg, with a time span of roughly 10 days and amplitude of ~ 0.35 in I . It is interesting to note that our observations of V811 Cyg have a quiescent I of ~ 12.90 whereas Spogli et al. (2002) measured $I_C > 14.8$ in 1995. A likely interpretation is that we have observed a blend between V811 Cyg and another, brighter source. Although the light curve we identify with V811 Cyg is one of the variables that does not have a match with 2MASS, we do identify two sources in the full 2MASS catalog that lie within $10''$ of our coordinates for the object. These sources have $J = 14.090$, $J = 15.397$, and $J - H > 0$. A blend of these two objects in DAOPHOT/ALLSTAR into a single object can account for the ~ 12.90 quiescent I . Note that the coordinates for V811 Cyg in the GCVS are more than $10''$ from our coordinates for the object.

One interesting miscellaneous variable that has not previously been detected as a variable is HAT 199-1753, which shows a flarelike brightening by at least 0.08 mag over the course of 5 hours. Unfortunately, the light curve is interrupted by several bad nights.

5.5. Low-Amplitude Periodic Variables

As a test of our ability to detect very low amplitude periodic variables, we performed the Schwarzenberg-Czerny period-finding test (see § 5.3) on the 8949 light curves that had rms better than 10 mmag and $J_S < 1.0$. Using this scheme we selected an additional 71 light curves that had $P < 0.9$ days, and $\sigma_{\text{AoV}} > 3.5$ for the best period, and did not lie near the 1/2 or 1/3 harmonic of 1 day. We only selected objects that were more than 6 pixels from a variable in our catalog, to avoid issues of variability blending. We then analyzed these light curves by eye and selected a list of 29 probable low-amplitude pulsating variables. We show light curves for a few of these in Figure 19, some of which have full amplitudes approaching 10 mmag.

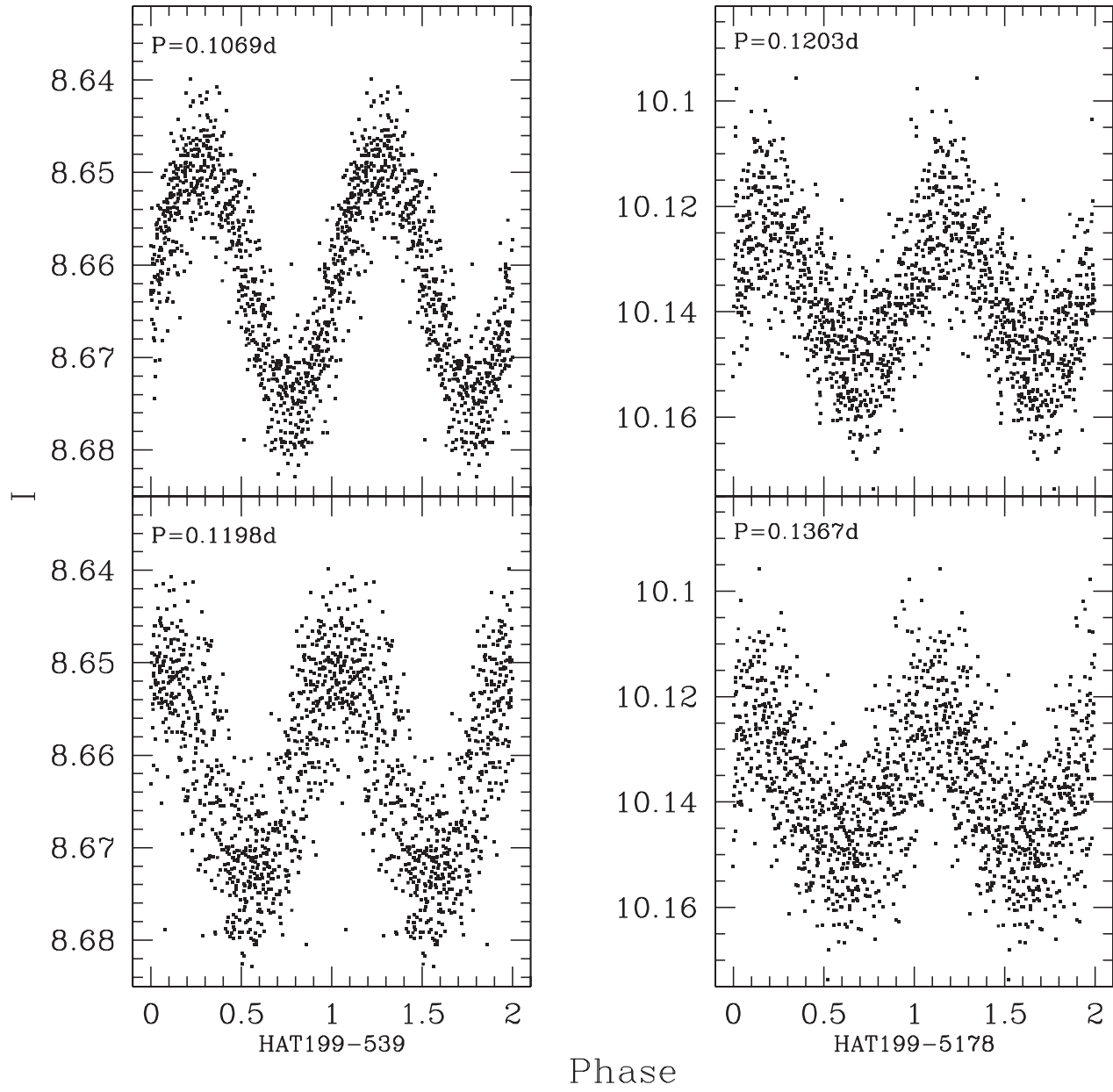


FIG. 17.—Light curves of HAT 199-539 (*left*) and HAT 199-5178 (*right*), two short-period pulsating variables that show multiple, nonharmonic periods. HAT 199-539 has periods of 0.1069 and 0.1198 days; HAT 199-5178 has periods of 0.1203 and 0.1367 days.

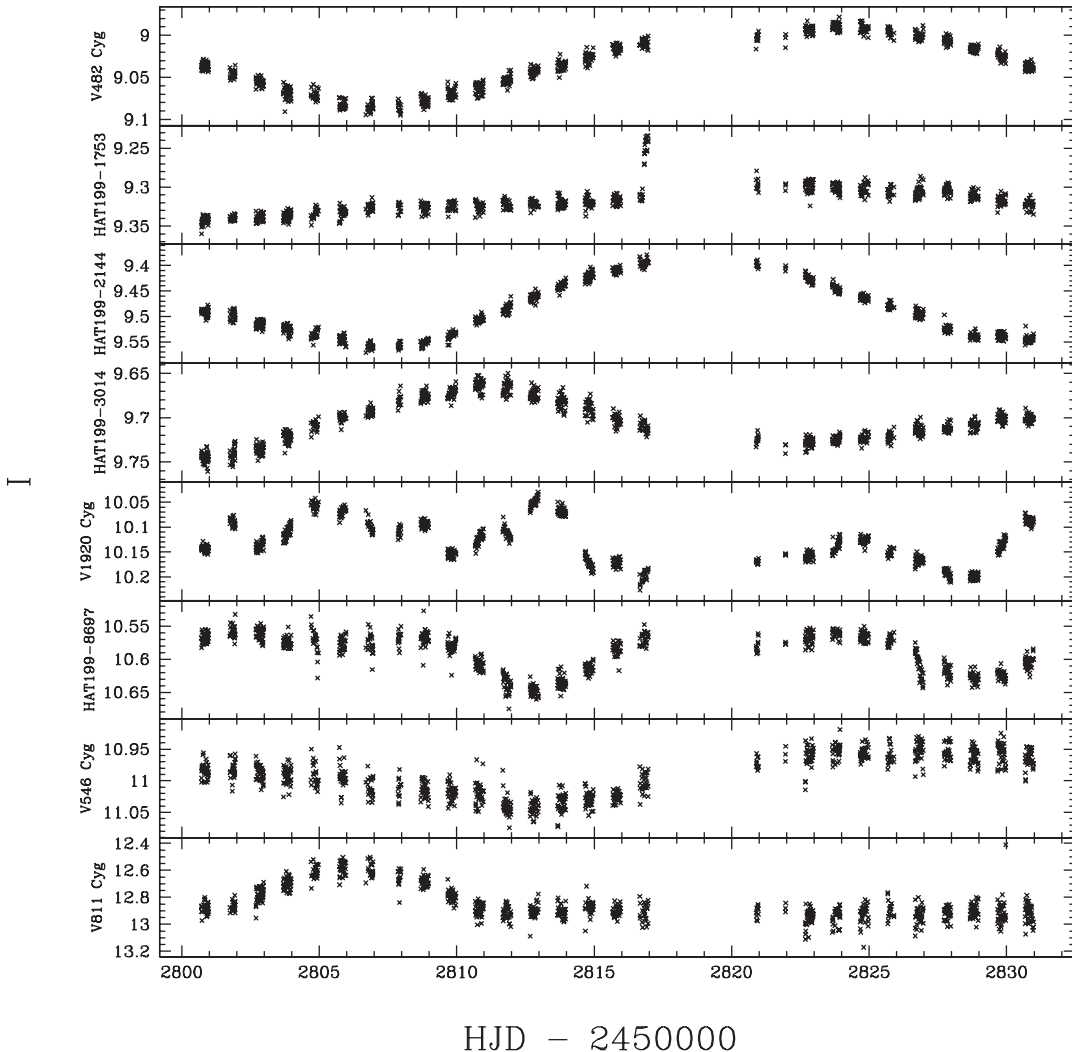
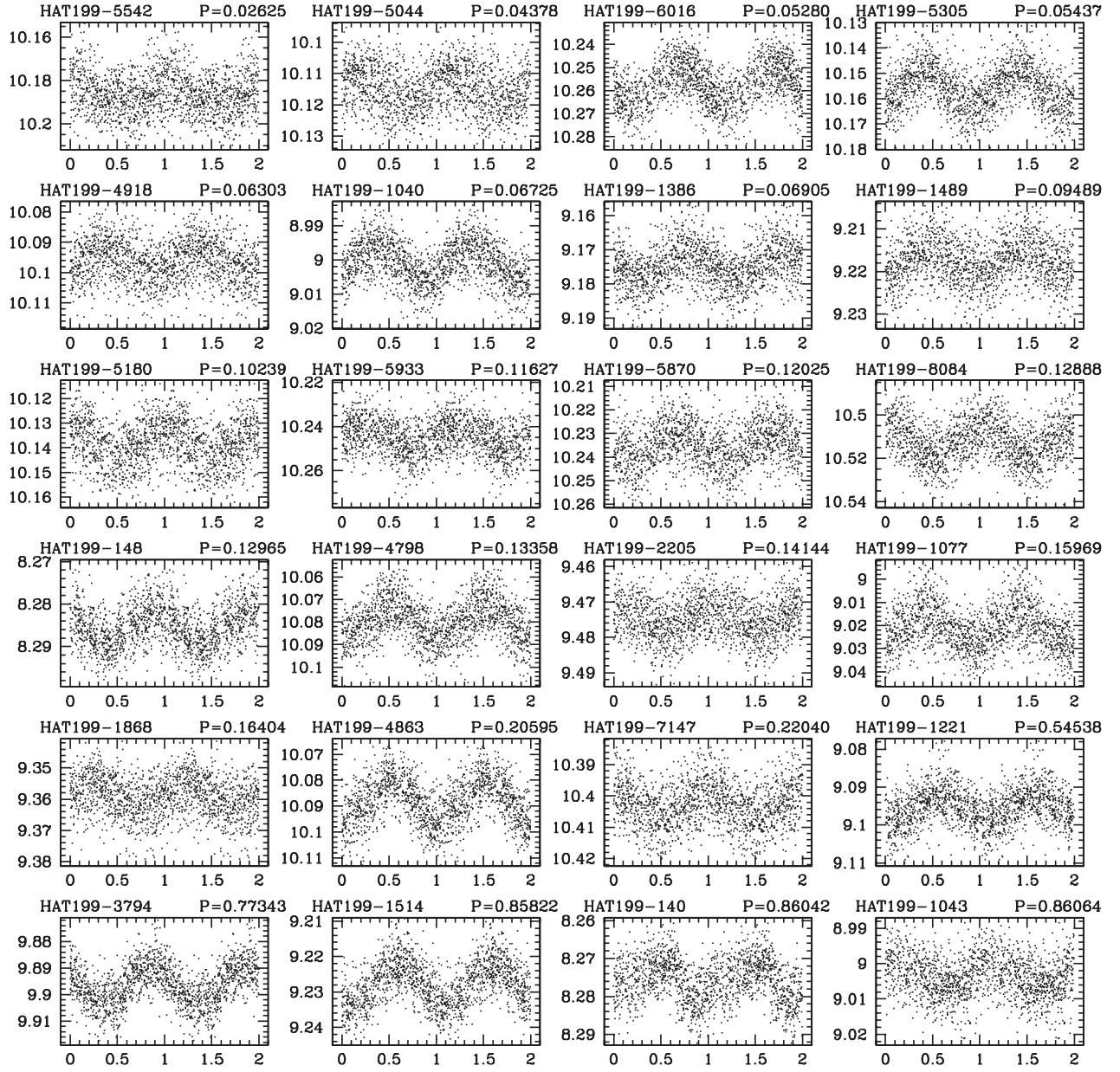


FIG. 18.—The *I*-band light curves for eight of the 240 miscellaneous variables in our catalog.

I



Phase

FIG. 19.—The *I*-band light curves of 24 low-amplitude periodic variables selected using the Schwarzenberg-Czerny algorithm.

This is not a systematic search for these variables; we present the results simply to demonstrate our capability of finding very low amplitude variables in a high-density field. We will continue observations of this field and present results from a systematic search for transits and other low-amplitude variability in a future paper.

6. CONCLUSION

By using image subtraction photometry, we have obtained light curves for over 98,000 objects in a single field near the Galactic plane. From these light curves we have identified 1617 variable stars with amplitudes greater than ~ 0.032 mag, of which 1439 are new. These include 1026 new LPVs, 176 new periodic variables, and 237 new miscellaneous variables. The fact that 89% of the variables were previously undetected further demonstrates the vast number of variables yet to be discovered even among fairly bright stars in our Galaxy (Paczyński 1997).

We will continue our observations of this field in the hopes of detecting planetary transits, as well as other low-amplitude variables, by means of extending our baseline. Using rudimentary selection techniques we have already identified as many as 29 periodic variables with amplitudes less than 0.05 mag. Besides the detection of low-amplitude variables, future observations should also help in determining the nature of the variables we have already discovered.

We gratefully acknowledge G. Pojmanski for his excellent “lc” program, W. Pych for his “fwhm” program, J. Devor for his period-finding code, P. Berlind, M. Calkins, and T. Matheson for obtaining and analyzing spectra of V1171 Cyg, D. Latham and N. Evans for helpful discussions, A. Bonanos, B. Mochejska, and C. Alard for their help with the ISIS photometric package, and P. Wils for his help with matching to the GCVS and NSV. We are grateful to C. Akerlof and the ROTSE project for the long-term loan of the lens used in the HAT-5 telescope. We also thank R. Lupton for his help and useful suggestions in refereeing this paper. This research has made use of the SIMBAD database, operated at CDS, Strasbourg, France. J. D. H. is funded by a National Science Foundation Graduate Student Research Fellowship. Partial support for the HAT project has been provided through NASA grant NAG 5-10854.

APPENDIX A

RUNNING IMAGE SUBTRACTION

To select a reference for alignment, we measured the FWHM values of all the images and then chose an image that had one of the smallest FWHMs, circular profiles, and good spatial overlap with the remaining images. At this point we also examined images with extreme values for FWHM (typically frames for which the program failed). Many of these turned out to be partially obscured by clouds or have irregular background patterns whose cause could not always be determined. These images were removed before proceeding with registration and subtraction.

Before proceeding with subtraction, we had to establish a set of subtraction parameters. These parameters include the number of independent regions into which to divide the images (`sub_x` and `sub_y`), the form of the kernel to use (including

the number of Gaussians, the “width” of the Gaussians, the orders of the polynomials associated with each Gaussian, the order of the polynomial used to fit spatial variations in the kernel, and the order of the polynomial used to fit spatial variations in the background), and the sizes (in pixels) of the regions used for fitting the kernel (`half_stamp_size`), as well as for performing the PSF transformation with the kernel (`half_mesh_size`). We first created a preliminary reference image from 30 of the lowest FWHM images, using a trial guess for the parameters. We then ran the ISIS routine “`subtract.csh`” using several permutations of the parameters (we varied the number of subregions, and the degree of background and spatial variations). For each permutation we calculated the standard deviation and mean of the subtracted images. We then chose the set of parameters that produced the lowest average standard deviation and mean. These include internally dividing each frame into 25 independent subframes (`sub_x = sub_y = 5`), using a first-order polynomial to fit the background variations and a first-order polynomial to fit the spatial variations in the kernel, fitting with three Gaussians, which had “widths” of 0.7, 2.0, and 4.0, respectively, and associated polynomials of order 6, 4, and 3, respectively, and choosing a `half_mesh_size` of 11 pixels and a `half_stamp_size` of 19 pixels. The internal subdivision is the most important parameter in our case. This is because the ISIS implementation of image subtraction assumes flux conservation over the whole field from image to image. For a wide FOV, this does not generally hold (for example, because of differential atmospheric extinction over the field). It becomes necessary to subdivide the field into regions over which the flux conservation assumption holds within the limits set by photon noise and sky background. We empirically find that subdividing into more than 25 sections yields negligible improvement to the standard deviation of the subtracted images (and the light curves of a selected sample of stars), while significantly increasing the computation time.

After obtaining a final reference image (composed of 47 images) for subtraction, we performed subtraction on all the images. At this point we sorted the subtracted images by standard deviation and mean, examining images with large standard deviations or means significantly different from zero. This procedure allowed us to identify images with subtle cloud patterns, etc., which might contaminate the photometry. Since image subtraction assumes that the flux of all stars scales by a constant from image to image, any complex background variations or clouds will yield significant residuals over an entire subregion of the subtracted image. The ease with which very subtle differences in images can be identified is one advantage of using image subtraction over methods to directly measure photometry on original images.

After cleaning, we were left with 800 out of 935 images on which to proceed with photometry.

APPENDIX B PERFORMING PHOTOMETRY

We obtained the light curves for 98,000 objects using the “`phot.csh`” routine contained in the ISIS package. This procedure first determines a PSF within a region of size `PSF_width` pixels on the reference image. This is done by taking the median profile of a stack of bright stars. The profiles for each star are interpolated (using a cubic B-spline) onto a common grid.

Spatial variations in the PSF are accounted for by splitting the image into several subareas. The routine then uses the best-fit kernel to transform it into the PSF for the subtracted image. It then measures the flux within a radius of `radphot` pixels from a specified location, weighting it by the PSF, and normalizes by the integral of the PSF squared over a region of radius `rad_aper` pixels. These difference-flux measurements can be converted into instrumental magnitude light curves for each object by using the flux on the reference image measured by DAOPHOT/ALLSTAR.

In converting from flux to magnitudes it is important to ensure that the flux measured by DAOPHOT/ALLSTAR is properly scaled to the flux measured by ISIS. The DAOPHOT/ALLSTAR fluxes correspond to the flux from PSF fitting using a zero point of 25.0 mag. In general, this flux is *not* equal to the total number of ADUs in the image contributed by the star in question. For a large aperture radius, the latter value is what is measured by “`phot.csh`.” To determine the scaling between the two “fluxes,” we perform an aperture correction as follows: After fitting a PSF to 98,000 stars in the field, we subtract a number of these stars from the reference image, leaving only a sparsely populated image. We then perform aperture photometry on the remaining stars in this sparse image (using a large aperture radius of 7 pixels). Comparing the aperture magnitudes with the PSF magnitudes, we find that the PSF magnitudes are consistently brighter by 0.19 mag. We can correct for this difference in scaling by using a zero point of $25.0 - 0.19 = 24.81$ mag for the DAOPHOT/ALLSTAR reference magnitudes of our program stars.

To optimize the ISIS photometry parameters, we ran the “`phot.csh`” procedure iteratively on a small subset of the 98,000 objects with magnitudes across the entire range. The parameters we varied include `rad_aper`, the `PSF_width`, and the inner and outer radii of the annulus for measuring the background (`rad1_bg` and `rad2_bg`). We related the parameters so that `PSF_width = 2 * rad_aper + 3`, `rad1_bg = 2 * rad_aper + 1`, and `rad2_bg = 2 * rad_aper + 6`. We also independently varied the radius for photometry (`radphot`), with little effect. We find that when the aperture radius is reduced below 7 pixels for our FWHM of ~ 3 pixels, the amplitude of the light curves (including the rms) is artificially reduced and the light

curves of variable stars (especially large-amplitude variable stars) become excessively noisy. We believe that this is the result inaccurately determining the PSF (increasing the noise of the variable stars) while simultaneously providing a flux that is not properly scaled (yielding lower amplitudes). For `rad_aper` greater than 7 pixels, the effect on the light curves is minimal, with a slight increase in the noise for the dim stars due to sampling more of the background. The final set of photometry parameters that we chose include `rad_aper = 7` pixels, `PSF_width = 17` pixels, `radphot = 3.0` pixels, `rad1_bg = 15.0` pixels, and `rad2_bg = 20.0` pixels.

After obtaining light curves for all the stars in our field, we checked to see if there were any remaining bad frames. To do this we calculated the rms of each light curve and then calculated, for each frame, the number of light curves for which the magnitude of that frame was more than 3σ from the mean. We identified 12 frames that were consistently “bad” in a large number of light curves. These frames were contaminated by clouds or airplane tracks or simply had subtracted images with substantial residuals and background gradients whose cause could not be identified on the original image. After removing these frames from every light curve, we were left with a total of 788 contributing frames. Several of the light curves contained an excessive number of outlier points as a result of lying near the edge of the field. To clean these light curves, we removed any point with a formal flux error less than 15 ADU as determined by the “`phot.csh`” routine (the average flux error being ~ 40 ADU for the dimmest stars). Some light curves also contained bad points as a result of lying near a saturated star. Because the profile of saturated stars is not fitted by the PSF, these stars yield significant residuals on the subtracted images. Since these residuals change from image to image, the contribution of this residual to the aperture of a nearby star changes. For dim stars, this effect dominates such that occasionally the difference flux measured by “`phot.csh`” is more negative than the flux of the star itself as measured by DAOPHOT. These can be eliminated by removing all points with negative-infinity magnitude from the light curves. The variability induced by proximity to saturated stars is difficult to distinguish from actual variability; we have attempted to account for these using templates to remove “bad” light curves (§ 4.4).

REFERENCES

- Alard, C. 2000, A&AS, 144, 363
- Alard, C., & Lupton, R. H. 1998, ApJ, 503, 325
- Alonso, R., Belmonte, J. A., & Brown, T. 2003, Ap&SS, 284, 13
- Bakos, G., Noyes, R. W., Kovács, G., Stanek, K. Z., Sasselov, D. D., & Domša, I. 2004, PASP, 116, 266
- Borucki, W. J., Caldwell, D., Koch, D. G., Webster, L. D., Jenkins, J. M., Ninkov, Z., & Shown, R. 2001, PASP, 113, 439
- . 2003, Proc. SPIE, 4854, 129
- Bouchy, F., Pont, F., Santos, N. C., Melo, C., Mayor, M., Queloz, D., & Udry, S. 2004, A&A, 421, L13
- Buccarelli, B., et al. 2001, A&A, 368, 335
- Couteau, P. 1981, A&AS, 43, 79
- Demircan, O., Müyesseroglu, Z., Selam, S. O., Derman, E., & Akalin, A. 1995, A&A, 297, 364
- Evans, N. R., Carpenter, K. C., Robinson, R., Kienzle, F., & Dekas, A. 2003, BAAS, 202, No. 39.06
- Fadeyev, Yu. A. 1990, MNRAS, 244, 225
- Groenewegen, M. A. T. 2004, A&A, in press (astro-ph/0404561)
- Horne, K. 2003, in ASP Conf. Ser. 294, Scientific Frontiers in Research on Extrasolar Planets, ed. D. Deming & S. Seager (San Francisco: ASP), 361
- Kaluzny, J., Stanek, K. Z., Krockenberger, M., Sasselov, D. D., Tonry, J. L., & Mateo, M. 1998, AJ, 115, 1016
- Khlopov, P. N., et al. 1998, Combined General Catalogue of Variable Stars (ed. 4.1; Moscow: Sternberg Astron. Inst.)
- Konacki, M., Torres, G., Jha, S., & Sasselov, D. D. 2003, Nature, 421, 507
- Konacki, M., et al. 2004, ApJ, 609, L37
- Kukarkin, B. V., et al. 1982, New Catalogue of Suspected Variable Stars (Moscow: Nauka)
- Lawson, W. A., & Cottrell, P. L. 1990, MNRAS, 242, 259
- Mochejska, B. J., Stanek, K. Z., Sasselov, D. D., & Szentgyorgyi, A. H. 2002, AJ, 123, 3460
- Mochejska, B. J., Stanek, K. Z., Sasselov, D. D., Szentgyorgyi, A. H., Westover, M., & Winn, J. N. 2004, AJ, 128, 312
- Morrison, K., & Willingale, G. P. H. 1987, MNRAS, 228, 819
- Paczyński, B. 1997, in Variable Stars and the Astrophysical Returns of the Microlensing Searches, ed. R. Ferlet, J.-P. Maillard, & B. Raban (Gif-sur-Yvette: Ed. Frontières), 357
- Parimucha, Š. 2003, Contrib. Astron. Obs. Skalnaté Pleso, 33, 99
- Perryman, M. A. C., et al. 1997, A&A, 323, L49
- Schwarzenberg-Czerny, A. 1996, ApJ, 460, L107
- Skrutskie, M. F., et al. 1997, in The Impact of Large-Scale Near-IR Sky Surveys, ed. F. Garzón, N. Epchtein, A. Omont, B. Burton, & P. Persi (Dordrecht: Kluwer), 25
- Spogli, C., Fiorucci, M., Tosti, G., Nucciarelli, G., Giretti, A. M., Monacelli, G., & Macchia, E. 2002, Inf. Bull. Variable Stars, No. 5240
- Stetson, P. B. 1987, PASP, 99, 191
- . 1992, JRASC, 86, 71
- . 1996, PASP, 108, 851

- Struve, O. 1946, *ApJ*, 104, 253
- Torres, G., Konacki, M., Sasselov, D. D., & Jha, S. 2004, *ApJ*, 609, 1071
- Udalski, A., Pietrzyński, G., Szymański, M., Kubiak, M., Żebruń, K., Soszyński, I., Szewczyk, O., & Wyrzykowski, Ł. 2003, *Acta Astron.*, 53, 133
- Udalski, A., Żebruń, K., Szymański, M., Kubiak, M., Soszyński, I., Szewczyk, O., Wyrzykowski, Ł., & Pietrzyński, G. 2002, *Acta Astron.*, 52, 115
- Wachmann, A. A. 1966, *Astron. Abh. Hamburger Sternw.*, 6, 281
- Wood, P. R. 2000, *Publ. Astron. Soc. Australia*, 17, 18
- Wood, P. R., et al. 1999, in *IAU Symp. 191, Asymptotic Giant Branch Stars*, ed. T. Le Bertre, A. Lèbre, & C. Waelkens (San Francisco: ASP), 151
- Woźniak, P. R. 2000, *Acta Astron.*, 50, 421
- Woźniak, P. R., et al. 2004, *AJ*, 127, 2436
- Yoon, T.-S., Honeycutt, R. K., Kaitchuck, R. H., & Schlegel, E. M. 1994, *PASP*, 106, 239
- Zavala, R. T., et al. 2002, *AJ*, 123, 450